INTRODUCTION [DRAFT]

Phased array antennas consist of a stationary spatial disposition of multiple coherently fed antennas that, acting on the phase of the excitations, allows to control the direction of the maximum gain achieved by the whole radiating structure. The array radiation pattern, as a result of far fields constructive and destructive interferences, is dependent on the relative phase shifts between the far fields produced by the antennas or *array elements*. An additional phase shift in the excitations simply modifies the directions of the constructive and destructive interferences, allowing a *beam steering* operation. Also, variable amplitude control of the excitations is often provided for pattern shaping. [1] [2] [3] [4] [5] [4]

These radiating structures are of a great importance in modern radar and communication systems. For example, modern fire control and artillery location radars make use of phased array antennas instead of mechanical beam steering systems, the latter ones having higher reaction times in target tracking and lower times to failure than mechanically fixed ones. Also, current cellular communication systems require, for the base stations, the ability to modify the radiation pattern in order to fit the illuminated zones to the desired ones and, if necessary, to hide undesired interferers by null-steering, that is the synthesis of a destructive interference in the direction of the interferer. These so-called *smart antennas* [6] are currently employed in the modern spatial diversity based communications techniques as the third generation cellular systems.

An accurate prediction of array parameters using numerical methods not only reduces the development cost and design period but also renders invaluable information to design engineers. For this purpose, several techniques like the method of mo-

ments (MoM), the finite-element method (FEM) and finite-difference time-domain (FDTD) are available. To accurately model the electromagnetic field behavior inside each array element and the mutual coupling between the elements, a three dimensional full-wave analysis is necessary. Furthermore, an accurate analysis of radiation problems is impossible without accurate modeling of the feeding structure. Due to its general formulation and versatility in geometrical modeling, the FEM appears to be the most suitable technique as an analysis tool.

However, the FEM requires very large computational and memory resources to allow fast design process. This is particularly true when the number of input parameters to consider in an effective design is high, and the simulations have to be iterated for each parameters set. Several techniques have been introduced in the last decade to face this problem. One of them, which will be presented in this thesis, splits the computations in two steps. The first, an *off-line* stage somewhat time and resources consuming but that needs to be run only once, provides an accurately chosen approximated model of the electromagnetic structure analyzed. The second, an *in-line* stage, allows a fast computation of the sought informations in front of variable input parameters, with an error dependent on the approximation made in the first step. These techniques are referred to as the *model order reduction* (MOR) techniques, and they have been successfully employed in multi-parameters wave guiding and scattering problems **CITATIONS of PAPERS**.

The purpose of the present thesis is to discuss the application of projection-based MOR techniques on frequency domain FEM simulations of planar phased arrays, leaving as inputs the excitations of the array elements and rapidly computing the far-zone fields patterns in front of a beamsteering process. In the first chapter, the electromagnetic radiation basics in a bounded medium will be reviewed. Then, in chapter 2, the process of finding a suitable approximation space for the model order reduction of phased arrays will be discussed. Finally, in chapter 3, the main projection-based MOR techniques nowadays involved in the electromagnetic research community will be viewed, with the application of the chosen techniques to the analysis of phased arrays.

CHAPTER 1

NEAR-ZONE TO FAR-ZONE FIELDS TRANSFORMATIONS

This chapter introduces the radiation from a generic distribution of sources located in a bounded medium, and the computation of the far-zone radiation patterns using the near fields given on a surface enclosing the sources. The fields will be derived by a direct integration of the sources.

As it has been widely used for its simplicity in the evaluation of a suitable approximation space for the reduction of the radiation model, the scalar wave Huygens' principle will be presented to treat the near-to-far fields transformations (N2F). Then, its formulation for vector fields will be given, being necessary to preserve the full-wave FEM formulation.

1.1 Radiation in a bounded medium

The problem of electromagnetic radiation from a generic distribution of current sources in a bounded medium relies on the solution of the Maxwell's equations [7]

$$\nabla \times \boldsymbol{E}(\boldsymbol{r},t) = -\frac{\partial}{\partial t}\boldsymbol{B}(\boldsymbol{r},t) \qquad \textit{Faraday's law,} \tag{1.1.1}$$

$$\nabla \times \boldsymbol{H}(\boldsymbol{r},t) = \frac{\partial}{\partial t}\boldsymbol{D}(\boldsymbol{r},t) + \boldsymbol{J}(\boldsymbol{r},t) \qquad \textit{Maxwell-Ampère's law,} \tag{1.1.2}$$

$$\nabla \cdot \boldsymbol{D}(\boldsymbol{r},t) = \rho(\boldsymbol{r},t) \qquad \textit{Poisson's equation,} \tag{1.1.3}$$

$$\nabla \cdot \boldsymbol{B}(\boldsymbol{r},t) = 0 \qquad \textit{Gauss' law for magnetism,} \tag{1.1.4}$$

where $\boldsymbol{E}$ is the *electric field intensity*, which carries the S.I.[1] units $[V/m]$, $\boldsymbol{H}$ the *magnetic field intensity* in $[A/m]$, $\boldsymbol{D}$ the *electric displacement* in $[C/m^2]$ (or $[As/m^3]$), $\boldsymbol{B}$ the *magnetic induction* in $[Wb/m^2]$ (or $[Vs/m^2]$), $\boldsymbol{J}$ the *electric current density* in $[A/m]$ and ρ the *electric charge density* in $[C/m^3]$ (or $[As/m^3]$). All these values are dependent on the position vector $\boldsymbol{r} \in \mathbb{R}^3$ and on the time variable $t \in \mathbb{R}$. Combining (1.1.2) and (1.1.3) by doing the divergence of the first, we obtain the *continuity equation*

$$\nabla \cdot \boldsymbol{J}(\boldsymbol{r},t) + \frac{\partial}{\partial t}\rho(\boldsymbol{r},t) = 0. \tag{1.1.5}$$

In order to solve this system of first order partial differential equations (PDEs) it is necessary to provide the *boundary conditions* and the *initial conditions*. Furthermore, as the number of equations is less than the number of unknowns, we need to supply the *constitutive relations*, which relates the electric displacement and the magnetic induction to the fields:

$$\boldsymbol{D}(\boldsymbol{r},t) = \overline{\overline{\epsilon}}(\boldsymbol{r},t)\cdot\boldsymbol{E}(\boldsymbol{r},t) + \overline{\overline{\xi}}(\boldsymbol{r},t)\cdot\boldsymbol{H}(\boldsymbol{r},t), \tag{1.1.6}$$

$$\boldsymbol{B}(\boldsymbol{r},t) = \overline{\overline{\zeta}}(\boldsymbol{r},t)\cdot\boldsymbol{E}(\boldsymbol{r},t) + \overline{\overline{\mu}}(\boldsymbol{r},t)\cdot\boldsymbol{H}(\boldsymbol{r},t), \tag{1.1.7}$$

where $\overline{\overline{\epsilon}}$, $\overline{\overline{\xi}}$, $\overline{\overline{\zeta}}$ and $\overline{\overline{\mu}}$ are dyadic tensors depending on the material in which the fields exist[2]. Furthermore, in presence of conductive materials, the electric field gives birth to an electric current density

$$\boldsymbol{J}^s(\boldsymbol{r},t) = \overline{\overline{\sigma}}(\boldsymbol{r},t)\cdot\boldsymbol{E}(\boldsymbol{r},t) \qquad \textit{Ohm's law,} \tag{1.1.8}$$

[1] Système International d'unités.

[2] The constitutive relations in (1.1.6-1.1.7) are stated in a very general form and can represent all the types of media, i.e. *isotropic*, *anisotropic*, *biisotropic* and *bianisotropic*.

where $\overline{\overline{\sigma}}$ is the *electric conductivity* dyadic tensor in $[S/m]$, and the superscript s on $\boldsymbol{J}^s(\boldsymbol{r},t)$ indicates that the current density is induced by the electric field. With this additional equation, the current $\boldsymbol{J}(\boldsymbol{r},t)$ in (1.1.2) is considered to be composed by an induced part, $\boldsymbol{J}^s(\boldsymbol{r},t)$, and by an impressed part, $\boldsymbol{J}^i(\boldsymbol{r},t)$, the latter actually being the source generating the electromagnetic fields.

Isn't it more common to denote the current density by J^c ?

For a bounded medium, the boundary conditions are those that ensure the fields extinction out of the domain investigated. This is possible by forcing the continuity of the fields at the interfaces between different media, and this is stated as[3], for a surface interfacing two media,

How can you achieve extinction without magnetic currents? (without disturbing the fields)
↳ you have to add magnetic charges and currents

$$\hat{\boldsymbol{n}} \times (\boldsymbol{E}_1(\boldsymbol{r},t) - \boldsymbol{E}_2(\boldsymbol{r},t)) = 0, \tag{1.1.9}$$

$$\hat{\boldsymbol{n}} \times (\boldsymbol{H}_1(\boldsymbol{r},t) - \boldsymbol{H}_2(\boldsymbol{r},t)) = \boldsymbol{J}_s(\boldsymbol{r},t), \tag{1.1.10}$$

$$\hat{\boldsymbol{n}} \cdot (\boldsymbol{D}_1(\boldsymbol{r},t) - \boldsymbol{D}_2(\boldsymbol{r},t)) = \rho_s(\boldsymbol{r},t), \tag{1.1.11}$$

$$\hat{\boldsymbol{n}} \cdot (\boldsymbol{B}_1(\boldsymbol{r},t) - \boldsymbol{B}_2(\boldsymbol{r},t)) = 0, \tag{1.1.12}$$

where $\hat{\boldsymbol{n}}$ is the unit vector normal to the surface, inwardly directed to the first region, $\boldsymbol{J}_s$ and ρ_s the *electric surface current density* in $[A/m]$ and *electric surface charge density* in $[C/m^2]$. By (1.1.10-1.1.12), we obtain surface current and charge densities that keep informations on the fields outside (region 2) of the region in which the Maxwell's equations are solved (region 1), as if the whole domain were unbounded.

For the radiation problem we need to solve in this chapter, we will consider *isotropic* (*homogeneous*) and *time-invariant* media, for which the dyadics relating the fields to the electric displacement and magnetic induction are scalar values. Thus, the constitutive relations become

$$\boldsymbol{D}(\boldsymbol{r},t) = \epsilon \boldsymbol{E}(\boldsymbol{r},t) = \epsilon_0 \epsilon_r \boldsymbol{E}(\boldsymbol{r},t), \tag{1.1.13}$$

$$\boldsymbol{B}(\boldsymbol{r},t) = \mu \boldsymbol{H}(\boldsymbol{r},t) = \mu_0 \mu_r \boldsymbol{H}(\boldsymbol{r},t), \tag{1.1.14}$$

where the constant $\epsilon_0 = 8.854 \cdot 10^{-12}$ $[F/m]$ is the *free-space permittivity*, ϵ_r the *relative permettivity*, a non-dimensional constant, $\mu_0 = 4\pi \cdot 10^{-7}$ $[H/m]$ is the *free-space*

[3] The continuity equations (1.1.10-1.1.12) are derived from an integral solution of the Maxwell's equations, assuming a connected volume made by a part of region 1 and a part of region 2, i.e. a closed surface crossing the boundary interface between the two regions.

permeability and μ_r the *relative permeability,* also non-dimensional. As we expect electromagnetic waves to be generated from the sources, we note their speed as $c = 1/\sqrt{\epsilon\mu} = c_0/\sqrt{\epsilon_r\mu_r}$ with $c_0 \approx 2.998 \cdot 10^8 \left[m/s\right]$ the *free-space speed of light.*

For the solution of Maxwell's equations there must be also given the initial conditions, that is, the values of the sources and the fields on the boundaries at $t = -\infty$. Our treatment will consider the frequency-domain formulation of the fields invoking the spectral representation of time dependent fields by the *Fourier integral theorem*

$$\psi(\boldsymbol{r},t) = \frac{1}{2\pi}\int_{-\infty}^{\infty} \tilde{\psi}(\boldsymbol{r},\omega)\mathrm{e}^{-j\omega t}\,d\omega.$$

Applying the *Fourier integral theorem* to the Maxwell's equations (1.1.1-1.1.4) we obtain

$$\nabla\times\tilde{\boldsymbol{E}}(\boldsymbol{r},\omega) = -j\omega\tilde{\boldsymbol{B}}(\boldsymbol{r},\omega), \tag{1.1.15}$$

$$\nabla\times\tilde{\boldsymbol{H}}(\boldsymbol{r},\omega) = j\omega\tilde{\boldsymbol{D}}(\boldsymbol{r},\omega)+\tilde{\boldsymbol{J}}(\boldsymbol{r},\omega), \tag{1.1.16}$$

$$\nabla\cdot\tilde{\boldsymbol{D}}(\boldsymbol{r},\omega) = \tilde{\rho}(\boldsymbol{r},\omega), \tag{1.1.17}$$

$$\nabla\cdot\tilde{\boldsymbol{B}}(\boldsymbol{r},\omega) = 0, \tag{1.1.18}$$

and to the continuity equation:

$$\nabla\cdot\tilde{\boldsymbol{J}}(\boldsymbol{r},\omega)+j\omega\tilde{\rho}(\boldsymbol{r},\omega)=0, \tag{1.1.19}$$

where we have used the Fourier integral of the time derivatives relation

$$\frac{\partial}{\partial t}\psi(\boldsymbol{r},t) \longleftrightarrow j\omega\tilde{\psi}(\boldsymbol{r},\omega),$$

ω being the angular frequency ($\omega = 2\pi f$ with f the frequency in [Hz]) and the symbol "~" over the frequency dependent function $\tilde{\psi}(\boldsymbol{r},\omega)$ denotes its spectrum (the *Fourier Transform*)

$$\tilde{\psi}(\boldsymbol{r},\omega) = \int_{-\infty}^{\infty} \psi(\boldsymbol{r},t)\mathrm{e}^{j\omega t}\,dt \qquad \in\mathbb{C},\ \forall\omega\in\mathbb{R}.$$

The spectral formulation allows us to neglect the initial conditions, the spectrum being computed by an integral over the entire domain of t ($t\in\mathbb{R}$). Also, with the spectral representation, the constitutive relations in isotropic media become

$$\tilde{\boldsymbol{D}}(\boldsymbol{r},\omega) = \epsilon\tilde{\boldsymbol{E}}(\boldsymbol{r},\omega), \tag{1.1.20}$$

$$\tilde{\boldsymbol{B}}(\boldsymbol{r},\omega) = \mu\tilde{\boldsymbol{H}}(\boldsymbol{r},\omega). \tag{1.1.21}$$

1.1.1 Symmetrized form of the Maxwell's equations

Before we face the problem of radiation in a bounded medium, it is interesting, for a mathematical problem solving point of view, to introduce the *symmetrized form of the Maxwell's equations.* Let us suppose there exist in nature, as we can find electric charges, *magnetic charges,* thus *magnetic charge densities* $\tilde{\rho}_m(\boldsymbol{r},\omega)$, and the motion of these charges would lead to *magnetic current densities* $\tilde{\boldsymbol{J}}_m(\boldsymbol{r},\omega)$. The S.I. units we should give to those values are, respectively, $[Vs/m^3]$ and $[V/m^2]$, for symmetry reasons. Furthermore, as a stationary electric charge leads to a diverging electric field and a moving one to a rotating magnetic field, a magnetic charge gives birth to a diverging magnetic field and a moving one to a rotating electric field (*Duality principle*). With these new entities, the Maxwell's equations would become

$$\nabla\times\tilde{\boldsymbol{E}}(\boldsymbol{r},\omega) = -j\omega\tilde{\boldsymbol{B}}(\boldsymbol{r},\omega)-\tilde{\boldsymbol{J}}_m(\boldsymbol{r},\omega), \tag{1.1.22}$$

$$\nabla\times\tilde{\boldsymbol{H}}(\boldsymbol{r},\omega) = j\omega\tilde{\boldsymbol{D}}(\boldsymbol{r},\omega)+\tilde{\boldsymbol{J}}(\boldsymbol{r},\omega), \tag{1.1.23}$$

$$\nabla\cdot\tilde{\boldsymbol{D}}(\boldsymbol{r},\omega) = \tilde{\rho}(\boldsymbol{r},\omega), \tag{1.1.24}$$

$$\nabla\cdot\tilde{\boldsymbol{B}}(\boldsymbol{r},\omega) = \tilde{\rho}_m(\boldsymbol{r},\omega). \tag{1.1.25}$$

There would also be a continuity equation for magnetic charges

$$\nabla\cdot\tilde{\boldsymbol{J}}_m(\boldsymbol{r},\omega)+j\omega\tilde{\rho}_m(\boldsymbol{r},\omega)=0, \tag{1.1.26}$$

and the continuity of the fields at the interface between media would become

$$\hat{\boldsymbol{n}}\times(\tilde{\boldsymbol{E}}_1(\boldsymbol{r},\omega)-\tilde{\boldsymbol{E}}_2(\boldsymbol{r},\omega)) = -\tilde{\boldsymbol{J}}_{ms}(\boldsymbol{r},\omega), \tag{1.1.27}$$

$$\hat{\boldsymbol{n}}\times(\tilde{\boldsymbol{H}}_1(\boldsymbol{r},\omega)-\tilde{\boldsymbol{H}}_2(\boldsymbol{r},\omega)) = \tilde{\boldsymbol{J}}_s(\boldsymbol{r},\omega), \tag{1.1.28}$$

$$\hat{\boldsymbol{n}}\cdot(\tilde{\boldsymbol{D}}_1(\boldsymbol{r},\omega)-\tilde{\boldsymbol{D}}_2(\boldsymbol{r},\omega)) = \tilde{\rho}_s(\boldsymbol{r},\omega), \tag{1.1.29}$$

$$\hat{\boldsymbol{n}}\cdot(\tilde{\boldsymbol{B}}_1(\boldsymbol{r},\omega)-\tilde{\boldsymbol{B}}_2(\boldsymbol{r},\omega)) = \tilde{\rho}_{ms}(\boldsymbol{r},\omega), \tag{1.1.30}$$

$\boldsymbol{J}_{ms}$ and ρ_{ms} being, respectively, the *magnetic surface current density* in $[V/m]$ and the *magnetic surface charge density* in $[Wb/m^2]$. Despite there is no physical proof of existence of magnetic monopoles, the symmetrized form of this new set of equations governing the electromagnetic phenomena represent, as we will see, a powerful tool

for the near to far fields transformations. In effect, it will be possible to consider the only currents, electric and magnetic, to preserve the continuity of the fields at the boundaries, simplifying in this way the computations.

1.1.2 The wave equation

The solutions $\tilde{\boldsymbol{E}}(\boldsymbol{r},\omega)$ and $\tilde{\boldsymbol{H}}(\boldsymbol{r},\omega)$ of the symmetrized Maxwell equations (1.1.22-1.1.25), using the constitutive relations (1.1.20-1.1.21), are fields continuously differentiable within the domain investigated. These fields can also be computed using the *frequency-domain wave equations* for electric and magnetic fields, obtained combining the curls of equations (1.1.22) and (1.1.23) and the constitutive relations (1.1.20-1.1.21),

$$\nabla\times\nabla\times\tilde{\boldsymbol{E}}(\boldsymbol{r},\omega)-k^2\tilde{\boldsymbol{E}}(\boldsymbol{r},\omega) = -\nabla\times\tilde{\boldsymbol{J}}_m(\boldsymbol{r},\omega)-j\omega\mu\tilde{\boldsymbol{J}}(\boldsymbol{r},\omega), \quad (1.1.31)$$

$$\nabla\times\nabla\times\tilde{\boldsymbol{H}}(\boldsymbol{r},\omega)-k^2\tilde{\boldsymbol{H}}(\boldsymbol{r},\omega) = \nabla\times\tilde{\boldsymbol{J}}(\boldsymbol{r},\omega)-j\omega\epsilon\tilde{\boldsymbol{J}}_m(\boldsymbol{r},\omega), \quad (1.1.32)$$

where $k=\omega\sqrt{\epsilon\mu}=\omega/c=2\pi/\lambda$, with λ the wavelength, is the *wavenumber*. The solution of these second-order PDEs are the same as the ones of the first-order Maxwell's PDEs, as long as the fields are spatially twice differentiable within the same domain.

Using the equivalence [7]

$$\nabla\times\nabla\times\boldsymbol{\Omega}=\nabla(\nabla\cdot\boldsymbol{\Omega})-\nabla\cdot(\nabla\boldsymbol{\Omega})=\nabla(\nabla\cdot\boldsymbol{\Omega})-\nabla^2\boldsymbol{\Omega} \quad (1.1.33)$$

and the constitutive relations to express the equations (1.1.24 - 1.1.25) in the form

$$\nabla\cdot\tilde{\boldsymbol{E}}(\boldsymbol{r},\omega) = \frac{1}{\epsilon}\tilde{\rho}(\boldsymbol{r},\omega), \quad (1.1.34)$$

$$\nabla\cdot\tilde{\boldsymbol{H}}(\boldsymbol{r},\omega) = \frac{1}{\mu}\tilde{\rho}_m(\boldsymbol{r},\omega), \quad (1.1.35)$$

the wave equations (1.1.32-1.1.32) can be rewritten in the *Helmholtz form* as follows

$$(\nabla^2+k^2)\tilde{\boldsymbol{E}}(\boldsymbol{r},\omega) = j\omega\mu\tilde{\boldsymbol{J}}(\boldsymbol{r},\omega)+\frac{1}{\epsilon}\nabla\tilde{\rho}(\boldsymbol{r},\omega)+\nabla\times\tilde{\boldsymbol{J}}_m(\boldsymbol{r},\omega), \quad (1.1.36)$$

$$(\nabla^2+k^2)\tilde{\boldsymbol{H}}(\boldsymbol{r},\omega) = j\omega\epsilon\tilde{\boldsymbol{J}}_m(\boldsymbol{r},\omega)+\frac{1}{\mu}\nabla\tilde{\rho}_m(\boldsymbol{r},\omega)-\nabla\times\tilde{\boldsymbol{J}}(\boldsymbol{r},\omega). \quad (1.1.37)$$

These equations can be solved, with the previously stated boundary conditions, considering each component $\tilde{\psi}(\boldsymbol{r},\omega)$ of the fields separately[4], and this leads to the solution of a set of three non-homogeneous differential equations for each field, the *scalar Helmholtz wave equations*

$$(\nabla^2 + k^2)\tilde{\psi}(\boldsymbol{r},\omega) \;=\; -\tilde{S}(\boldsymbol{r},\omega), \tag{1.1.38}$$

where the sources terms of the right-hand sides of (1.1.36-1.1.37) have been compacted into the scalar term $\tilde{S}(\boldsymbol{r},\omega)$.

1.1.3 Scalar Huygens' principle

Let us face now the problem of radiation in a bounded medium finding a solution to the scalar wave equation [7]. The figure 1.1 illustrates the geometry of the problem:

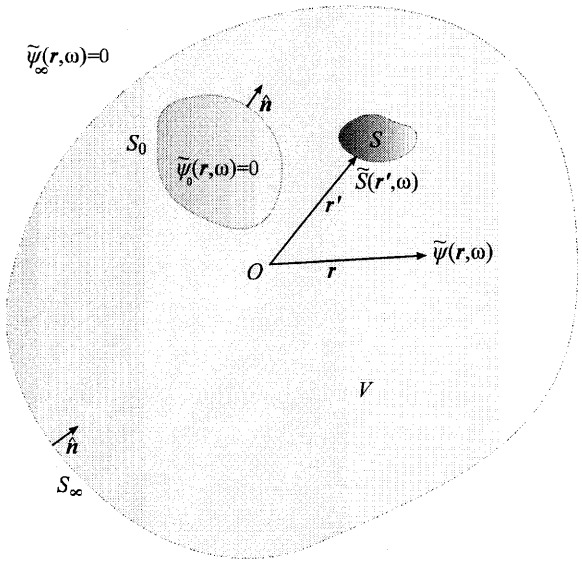

Figure 1.1: Electromagnetic radiation by arbitrary source distribution in an bounded medium.

a volume V, determined by the space between the arbitrarily shaped surfaces S_0 and S_∞, contains an arbitrarily shaped source distribution S, and the vector $\boldsymbol{r}'$ points to

[4] According to the fact that fields and currents are vector functions of the space such that and can be expressed by mean of a basis in $\mathbb{R}^3$, for example by a linear combination of vectors parallel to the unit vectors of a Cartesian coordinates system.

the *infinitesimal source element* or *point source* $\tilde{S}(\boldsymbol{r}',\omega)$. The unit vector $\hat{\boldsymbol{n}}$ normal to the surfaces is chosen to be inwardly directed to V.

As previously said, the solution of this problem consists of solving the frequency domain Helmholtz wave equation (1.1.38) where $\psi(\boldsymbol{r}';\omega)$ is any of the components of the vector fields. To solve $\psi(\boldsymbol{r};\omega)$ we must know the field produced by a point source, assuming that the fields are given by the superposition[5] of the fields produced by each point source. This is the *Green's function* denoted $G(\boldsymbol{r}|\boldsymbol{r}';\omega)$ and corresponds to the field produced in $\boldsymbol{r}$ by a point source located in $\boldsymbol{r}'$ [10]

$$(\nabla^2 + k^2)G(\boldsymbol{r}|\boldsymbol{r}';\omega) = \delta(\boldsymbol{r}-\boldsymbol{r}'), \tag{1.1.39}$$

where δ is the Dirac delta function of the position $\boldsymbol{r}$.

Furthermore, a solution to the Helmholtz equation (1.1.38) can be obtained using the *Green's second identity* [7] based on the following identity

$$\nabla\cdot(\Phi\nabla\Psi - \Psi\nabla\Phi) = \Phi\nabla^2\Psi - \Psi\nabla^2\Phi, \tag{1.1.40}$$

where Φ and Ψ are arbitrary scalar fields, then integrating over the volume V with respect to the dummy variable $\boldsymbol{r}'$ and using the *divergence theorem*

$$\int_V \nabla'\cdot\boldsymbol{\Omega}\, dV' = -\oint_S \boldsymbol{\Omega}\cdot\hat{\boldsymbol{n}}\, dS', \tag{1.1.41}$$

where $\boldsymbol{\Omega}$ is a vector-valued function of the space[6] and $\hat{\boldsymbol{n}}$ points inward to V. Assuming $\Phi = \tilde{\psi}(\boldsymbol{r}';\omega)$ and $\Psi = G(\boldsymbol{r}|\boldsymbol{r}';\omega)$, we obtain

$$\int_V \left[\tilde{\psi}(\boldsymbol{r}';\omega)\nabla'^2 G(\boldsymbol{r}|\boldsymbol{r}';\omega) - G(\boldsymbol{r}|\boldsymbol{r}';\omega)\nabla'^2\tilde{\psi}(\boldsymbol{r}';\omega)\right] dV' = -\oint_S \left[\tilde{\psi}(\boldsymbol{r}';\omega)\nabla' G(\boldsymbol{r}|\boldsymbol{r}';\omega) - G(\boldsymbol{r}|\boldsymbol{r}';\omega)\nabla'\tilde{\psi}(\boldsymbol{r}';\omega)\right]\cdot\hat{\boldsymbol{n}}\, dS'. \tag{1.1.42}$$

Since $\frac{\partial}{\partial n'} = \hat{\boldsymbol{n}}\cdot\nabla'$, we can rewrite the right-hand side of (1.1.42) in the following manner

$$\int_V \left[\tilde{\psi}(\boldsymbol{r}';\omega)\nabla'^2 G(\boldsymbol{r}|\boldsymbol{r}';\omega) - G(\boldsymbol{r}|\boldsymbol{r}';\omega)\nabla'^2\tilde{\psi}(\boldsymbol{r}';\omega)\right] dV' = -\oint_{S_0+S_\infty} \left[\tilde{\psi}(\boldsymbol{r}';\omega)\frac{\partial G(\boldsymbol{r}|\boldsymbol{r}';\omega)}{\partial n'} - G(\boldsymbol{r}|\boldsymbol{r}';\omega)\frac{\partial\tilde{\psi}(\boldsymbol{r}';\omega)}{\partial n'}\right] dS' \tag{1.1.43}$$

[5] According to the linearity property of Maxwell's equations, in particular of the operators $\nabla\cdot$, $\nabla\times$ and ∇.

[6] Notice that the gradient of a scalar function of the space is a vector function.

Then, applying the substitutions

$$\nabla^2\tilde{\psi}(\boldsymbol{r}';\omega) = -k^2\tilde{\psi}(\boldsymbol{r}';\omega) - \tilde{S}(\boldsymbol{r}',\omega)$$

and

$$\nabla^2 G(\boldsymbol{r}|\boldsymbol{r}';\omega) = -k^2 G(\boldsymbol{r}|\boldsymbol{r}';\omega) - \delta(\boldsymbol{r}-\boldsymbol{r}')$$

derived from (1.1.38-1.1.39) in the left-hand side of equation (1.1.43), we obtain

$$\begin{aligned}\int_V \Big[\tilde{\psi}(\boldsymbol{r}';\omega)\left(-k^2 G(\boldsymbol{r}|\boldsymbol{r}';\omega) - \delta(\boldsymbol{r}-\boldsymbol{r}')\right) - \\ G(\boldsymbol{r}|\boldsymbol{r}';\omega)\left(-k^2\tilde{\psi}(\boldsymbol{r}';\omega) - \tilde{S}(\boldsymbol{r}';\omega)\right)\Big] dV' = \\ -\oint_{S_0+S_\infty}\left[\tilde{\psi}(\boldsymbol{r}';\omega)\frac{\partial G(\boldsymbol{r}|\boldsymbol{r}';\omega)}{\partial n'} - G(\boldsymbol{r}|\boldsymbol{r}';\omega)\frac{\partial\tilde{\psi}(\boldsymbol{r}';\omega)}{\partial n'}\right] dS'. \quad (1.1.44)\end{aligned}$$

Being equivalent, the terms with the wavenumber k vanish, and the sifting property of the Dirac delta gives the following equation

$$\begin{aligned}\tilde{\psi}(\boldsymbol{r};\omega) &= \int_V G(\boldsymbol{r}|\boldsymbol{r}';\omega)\tilde{S}(\boldsymbol{r}';\omega)\, dV' + \\ &\oint_{S_0+S_\infty}\left[\tilde{\psi}(\boldsymbol{r}';\omega)\frac{\partial G(\boldsymbol{r}|\boldsymbol{r}';\omega)}{\partial n'} - G(\boldsymbol{r}|\boldsymbol{r}';\omega)\frac{\partial\tilde{\psi}(\boldsymbol{r}';\omega)}{\partial n'}\right] dS', \quad (1.1.45)\end{aligned}$$

if $\boldsymbol{r}$ is chosen to lie within V, otherwise $\tilde{\psi}(\boldsymbol{r};\omega) = 0$.

The integral over S_∞ vanishes when $\boldsymbol{r}' \to \infty$, as the field $\tilde{\psi}(\boldsymbol{r};\omega)$ and its derivative go to zero for the *Sommerfeld's radiation conditions*[7] expressed by the following limits

$$\lim_{r\to\infty}\tilde{\psi}(\boldsymbol{r};\omega) = 0, \quad (1.1.46)$$

$$\lim_{r\to\infty}\left[jk\tilde{\psi}(\boldsymbol{r};\omega) + \frac{\partial}{\partial r}\tilde{\psi}(\boldsymbol{r};\omega)\right] = 0. \quad (1.1.47)$$

Removing the integral over S_∞ means that we are removing the outer bounding surface of V, letting the radiation externally unbounded, useful operation for the radiation pattern computation. Hence, the equation (1.1.45) becomes

$$\begin{aligned}\tilde{\psi}(\boldsymbol{r};\omega) = \int_V G(\boldsymbol{r}|\boldsymbol{r}';\omega)S(\boldsymbol{r}';\omega)dV' + \\ \oint_{S_0}\left[\tilde{\psi}(\boldsymbol{r}';\omega)\frac{\partial G(\boldsymbol{r}|\boldsymbol{r}';\omega)}{\partial n'} - G(\boldsymbol{r}|\boldsymbol{r}';\omega)\frac{\partial\tilde{\psi}(\boldsymbol{r}';\omega)}{\partial n'}\right] dS'. \quad (1.1.48)\end{aligned}$$

[7] These limits actually express the physically observable attenuation of the electromagnetic fields as we get away from the sources.

The equation (1.1.48) states that the field $\tilde{\psi}(\boldsymbol{r};\omega)$ within V ($V \equiv \mathbb{R}^3/\{V_{S_0}\}$), can be determined once one knows the source distribution S within V and the fields and their normal derivatives on S_0.

The problem of near-zone to far-zone fields transformations can be split into two parts. The first concerns in the determination of the near fields over an arbitrary surface S_C encompassing the whole sources distribution, that is computing the first integral of (1.1.48) to obtain the fields and their normal derivatives on S_C, such that the sources can be excluded from V in the second part. The second part uses the near fields and derivatives previously obtained to calculate the fields in V. This is the scalar Huygen's principle, stated in the second integral of (1.1.48), which says that all the necessary informations about the sources enclosed is kept in the fields they produce on the enclosing surface. The near-to-far transformations with scalar fields will be discussed in section 1.2. We first proceed with the extension of the radiation in an bounded medium to vector fields.

1.1.4 Vector Huygens' principle

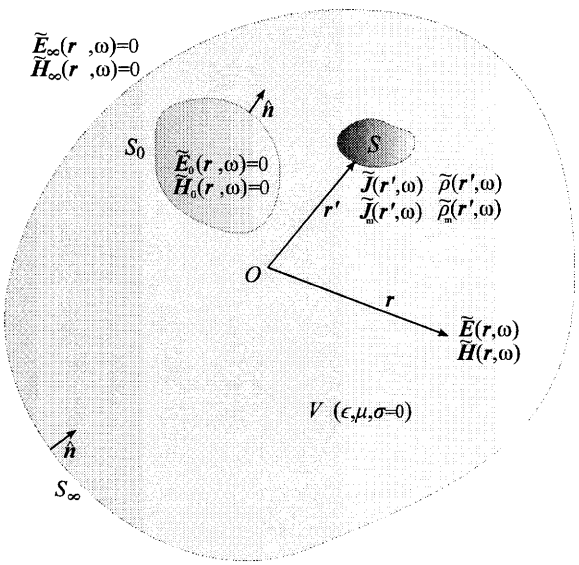

Figure 1.2: Electromagnetic radiation by arbitrary currents and charges distribution in a bounded medium.

Proceeding in the same manner as for the scalar Huygens' principle, we now use the *Green's second identity* (1.1.40) extended to vector fields to compute the electric field in the bounded medium depicted in figure 1.2. We obtain

$$\int_V \left[\tilde{\boldsymbol{E}}(\boldsymbol{r}';\omega)\nabla'^2 G(\boldsymbol{r}|\boldsymbol{r}';\omega) - G(\boldsymbol{r}|\boldsymbol{r}';\omega)\nabla'^2\tilde{\boldsymbol{E}}(\boldsymbol{r}';\omega)\right] dV' =$$
$$-\oint_{S_0+S_\infty} \left[\tilde{\boldsymbol{E}}(\boldsymbol{r}';\omega)\left(\hat{\boldsymbol{n}}\cdot\nabla' G(\boldsymbol{r}|\boldsymbol{r}';\omega)\right) - G(\boldsymbol{r}|\boldsymbol{r}';\omega)\left(\hat{\boldsymbol{n}}\cdot\nabla'\tilde{\boldsymbol{E}}(\boldsymbol{r}';\omega)\right)\right] dS', \quad (1.1.49)$$

where $\hat{\boldsymbol{n}}$ is inwardly directed to V. We now apply to the left-hand side integrand of (1.1.49) the substitutions

$$\nabla^2\tilde{\boldsymbol{E}}(\boldsymbol{r},\omega) = -k^2\tilde{\boldsymbol{E}}(\boldsymbol{r},\omega) + j\omega\mu\tilde{\boldsymbol{J}}(\boldsymbol{r},\omega) + \frac{1}{\epsilon}\nabla\tilde{\rho}(\boldsymbol{r},\omega) + \nabla\times\tilde{\boldsymbol{J}}_m(\boldsymbol{r},\omega)$$

and

$$\nabla^2 G(\boldsymbol{r}|\boldsymbol{r}';\omega) = -k^2 G(\boldsymbol{r}|\boldsymbol{r}';\omega) - \delta(\boldsymbol{r}-\boldsymbol{r}')$$

respectively derived from (1.1.36) and (1.1.39) to obtain the equation

$$\int_V \left[-\tilde{\boldsymbol{E}}\,\delta(\boldsymbol{r}-\boldsymbol{r}') - G\left(j\omega\mu\tilde{\boldsymbol{J}} + \frac{1}{\epsilon}\nabla'\tilde{\rho} + \nabla'\times\tilde{\boldsymbol{J}}_m\right)\right] dV' =$$
$$-\oint_{S_0+S_\infty} \left[\tilde{\boldsymbol{E}}\left(\hat{\boldsymbol{n}}\cdot\nabla' G\right) - G\left(\hat{\boldsymbol{n}}\cdot\nabla'\tilde{\boldsymbol{E}}\right)\right] dS', \quad (1.1.50)$$

where, for compactness in notation, we have made the substitutions $\tilde{\boldsymbol{E}} = \tilde{\boldsymbol{E}}(\boldsymbol{r}';\omega)$, $G = G(\boldsymbol{r}|\boldsymbol{r}';\omega)$, $\tilde{\boldsymbol{J}} = \tilde{\boldsymbol{J}}(\boldsymbol{r}',\omega)$, $\tilde{\rho} = \tilde{\rho}(\boldsymbol{r}',\omega)$ and $\tilde{\boldsymbol{J}}_m = \tilde{\boldsymbol{J}}_m(\boldsymbol{r}',\omega)$. Once again, the terms with the wavenumber k have cancelled each other. The sifting property of the Dirac delta allows the calculation of the field $\tilde{\boldsymbol{E}}(\boldsymbol{r};\omega)$ in an arbitrary point of V (elsewhere null), and (1.1.50) becomes

$$\tilde{\boldsymbol{E}}(\boldsymbol{r};\omega) = -\int_V \left[G\left(j\omega\mu\tilde{\boldsymbol{J}} + \frac{1}{\epsilon}\nabla'\tilde{\rho} + \nabla'\times\tilde{\boldsymbol{J}}_m\right)\right] dV' +$$
$$\oint_{S_0+S_\infty} \left[\tilde{\boldsymbol{E}}\left(\hat{\boldsymbol{n}}\cdot\nabla' G\right) - G\left(\hat{\boldsymbol{n}}\cdot\nabla'\tilde{\boldsymbol{E}}\right)\right] dS'. \quad (1.1.51)$$

Using the integral theorems (respectively *gradient theorem* and *curl theorem*) [7]

$$\int_V \nabla'\Psi\, dV' = -\oint_S \Psi\cdot\hat{\boldsymbol{n}}\, dS', \quad (1.1.52)$$
$$\int_V \nabla'\times\boldsymbol{\Omega}\, dV' = -\oint_S \hat{\boldsymbol{n}}\times\boldsymbol{\Omega}\, dS', \quad (1.1.53)$$

with $\hat{\boldsymbol{n}}$ pointing inward to V, one can rewrite the first integral term of right-hand side of (1.1.51) as

$$-\int_V \left[j\omega\mu G\tilde{\boldsymbol{J}} + \frac{1}{\epsilon} G\nabla'\tilde{\rho} + G\nabla'\times\tilde{\boldsymbol{J}}_m \right] dV' = -\int_V \left[j\omega\mu G\tilde{\boldsymbol{J}} - \frac{1}{\epsilon}\tilde{\rho}\nabla' G + \tilde{\boldsymbol{J}}_m\times\nabla' G \right] dV' + \oint_{S_0+S_\infty} \left[\hat{\boldsymbol{n}}\frac{1}{\epsilon}\tilde{\rho}G + \hat{\boldsymbol{n}}\times\tilde{\boldsymbol{J}}_m G \right] dS', \tag{1.1.54}$$

where the vector identities [8]

$$\nabla(\Psi\Phi) = \Psi\nabla\Phi + \Phi\nabla\Psi, \tag{1.1.55}$$

$$\nabla\times(\Psi\boldsymbol{\Omega}) = \Psi\nabla\times\boldsymbol{\Omega} + \nabla\Phi\times\boldsymbol{\Omega}, \tag{1.1.56}$$

have been employed with $\Psi = G$, $\Phi = \tilde{\rho}$ and $\boldsymbol{\Omega} = \tilde{\boldsymbol{J}}_m$. Then, using the following vector identity [8]

$$\Psi(\hat{\boldsymbol{n}}\cdot\nabla\boldsymbol{\Omega}) - \boldsymbol{\Omega}(\hat{\boldsymbol{n}}\cdot\nabla\Psi) = [\hat{\boldsymbol{n}}\cdot\nabla(\Psi\boldsymbol{\Omega}) + \hat{\boldsymbol{n}}\times(\nabla\times(\Psi\boldsymbol{\Omega})) - \hat{\boldsymbol{n}}\nabla\cdot(\Psi\boldsymbol{\Omega})] + [\hat{\boldsymbol{n}}\Psi\nabla\cdot\boldsymbol{\Omega} - (\hat{\boldsymbol{n}}\times\boldsymbol{\Omega})\times\nabla\Psi - \Psi\hat{\boldsymbol{n}}\times(\nabla\times\boldsymbol{\Omega}) - (\hat{\boldsymbol{n}}\cdot\boldsymbol{\Omega})\nabla\Psi], \tag{1.1.57}$$

and assuming $\Psi = G$ and $\boldsymbol{\Omega} = \tilde{\boldsymbol{E}}$, the second integrand term in the right-hand side of (1.1.51) can be expressed as

$$\oint_{S_0+S_\infty} [\tilde{\boldsymbol{E}}(\hat{\boldsymbol{n}}\cdot\nabla' G) - G(\hat{\boldsymbol{n}}\cdot\nabla'\tilde{\boldsymbol{E}})]\, dS' = -\oint_{S_0+S_\infty} [\hat{\boldsymbol{n}}\cdot\nabla'(G\tilde{\boldsymbol{E}}) + \hat{\boldsymbol{n}}\times(\nabla'\times(G\tilde{\boldsymbol{E}}))\,\hat{\boldsymbol{n}}\nabla'\cdot(G\tilde{\boldsymbol{E}})]\, dS' + -\oint_{S_0+S_\infty} [\hat{\boldsymbol{n}}G\nabla'\cdot\tilde{\boldsymbol{E}} - (\hat{\boldsymbol{n}}\times\tilde{\boldsymbol{E}})\times\nabla' G - G\hat{\boldsymbol{n}}\times(\nabla'\times\tilde{\boldsymbol{E}}) - (\hat{\boldsymbol{n}}\cdot\tilde{\boldsymbol{E}})\nabla' G]\, dS'. \tag{1.1.58}$$

The integral theorem [8]

$$\oint_S (\hat{\boldsymbol{n}}\times\nabla')\times(\Psi\boldsymbol{\Omega})\, dS = 0 = \oint_S [\hat{\boldsymbol{n}}\times(\nabla'\times(\Psi\boldsymbol{\Omega})) + (\hat{\boldsymbol{n}}\cdot\nabla')(\Psi\boldsymbol{\Omega}) - \hat{\boldsymbol{n}}(\nabla'\cdot(\Psi\boldsymbol{\Omega}))]\, dS \tag{1.1.59}$$

allows us to neglect the first integral term in right-hand side of (1.1.58), and (1.1.51) can be expressed as

$$\tilde{\boldsymbol{E}}(\boldsymbol{r};\omega) = -\int_V \left[j\omega\mu G\tilde{\boldsymbol{J}} - \frac{1}{\epsilon}\tilde{\rho}\nabla' G + \tilde{\boldsymbol{J}}_m\times\nabla' G \right] dV' +$$

$$\oint_{S_0+S_\infty}\left[\hat{\boldsymbol{n}}\frac{1}{\epsilon}\tilde{\rho}G+\hat{\boldsymbol{n}}\times\tilde{\boldsymbol{J}}_m G\right]dS'-$$

$$\oint_{S_0+S_\infty}\left[\hat{\boldsymbol{n}}G\nabla'\cdot\tilde{\boldsymbol{E}}-(\hat{\boldsymbol{n}}\times\tilde{\boldsymbol{E}})\times\nabla'G-G\hat{\boldsymbol{n}}\times(\nabla'\times\tilde{\boldsymbol{E}})-(\hat{\boldsymbol{n}}\cdot\tilde{\boldsymbol{E}})\nabla'G\right]dS' \quad (1.1.60)$$

The divergence and curl of the electric field terms in the integrand of the third surface integral of right-hand side of (1.1.60) can be substituted, respectively, using the Poisson's equation (1.1.34) and the symmetrized Faraday's law (1.1.22) together with the constitutive equation of the magnetic field (1.1.21). As a result, the second integral of right-hand side of (1.1.60) vanishes and we obtain

$$\tilde{\boldsymbol{E}}(\boldsymbol{r};\omega)=\int_V\left[-j\omega\mu G\tilde{\boldsymbol{J}}+\frac{1}{\epsilon}\tilde{\rho}\nabla'G-\tilde{\boldsymbol{J}}_m\nabla'\times G\right]dV'+$$

$$\oint_{S_0+S_\infty}\left[-j\omega\mu G(\hat{\boldsymbol{n}}\times\tilde{\boldsymbol{H}})+(\hat{\boldsymbol{n}}\cdot\tilde{\boldsymbol{E}})\nabla'G+(\hat{\boldsymbol{n}}\times\tilde{\boldsymbol{E}})\times\nabla'G\right]dS', \quad (1.1.61)$$

where $\tilde{\boldsymbol{H}}=\tilde{\boldsymbol{H}}(\boldsymbol{r}';\omega)$. Then, considering the medium externally unbounded, that is letting the bounding surface S_∞ going far away from the sources positions and applying the *Sommerfeld's radiation conditions* for vector fields [7]

$$\lim_{r\to\infty} r\tilde{\boldsymbol{E}}(\boldsymbol{r};\omega) \;<\; \infty, \quad (1.1.62)$$

$$\lim_{r\to\infty} r\left[\zeta\hat{\boldsymbol{r}}\times\tilde{\boldsymbol{H}}(\boldsymbol{r};\omega)+\tilde{\boldsymbol{E}}(\boldsymbol{r};\omega)\right] \;=\; 0, \quad (1.1.63)$$

with $\zeta=\sqrt{\frac{\mu}{\epsilon}}\approx 376.73[\Omega]$ the *plane wave impedance*, we obtain the following equation for the electric field

$$\tilde{\boldsymbol{E}}(\boldsymbol{r};\omega)=\int_V\left[-j\omega\mu G\tilde{\boldsymbol{J}}+\frac{1}{\epsilon}\tilde{\rho}\nabla'G-\tilde{\boldsymbol{J}}_m\nabla'\times G\right]dV'+$$

$$\oint_{S_0}\left[-j\omega\mu G(\hat{\boldsymbol{n}}\times\tilde{\boldsymbol{H}})+(\hat{\boldsymbol{n}}\cdot\tilde{\boldsymbol{E}})\nabla'G+(\hat{\boldsymbol{n}}\times\tilde{\boldsymbol{E}})\times\nabla'G\right]dS'. \quad (1.1.64)$$

Proceeding analogously, we derive an equation for the magnetic field

$$\tilde{\boldsymbol{H}}(\boldsymbol{r};\omega) \;=\; \int_V\left[-j\omega\epsilon G\tilde{\boldsymbol{J}}_m+\frac{1}{\mu}\tilde{\rho}_m\nabla'G-\tilde{\boldsymbol{J}}\nabla'\times G\right]dV'+$$

$$\oint_{S_0}\left[j\omega\epsilon G(\hat{\boldsymbol{n}}\times\tilde{\boldsymbol{E}})+(\hat{\boldsymbol{n}}\cdot\tilde{\boldsymbol{H}})\nabla'G+(\hat{\boldsymbol{n}}\times\tilde{\boldsymbol{H}})\times\nabla'G\right]dS', \quad (1.1.65)$$

with the additional equivalence $\tilde{\rho}_m=\tilde{\rho}_m(\boldsymbol{r}',\omega)$. The radiation conditions corresponding to (1.1.65) are

$$\lim_{r\to\infty} r\tilde{\boldsymbol{H}}(\boldsymbol{r};\omega) \;<\; \infty, \quad (1.1.66)$$

Do you really need them? Are they not equivalent to (1.1.63)+(1.1.62) + Maxw. Eq.?

But they are correct and you can state them :-)

$$\lim_{r\to\infty} r\left[\zeta\tilde{\boldsymbol{H}}(\boldsymbol{r};\omega)-\hat{\boldsymbol{r}}\times\tilde{\boldsymbol{E}}(\boldsymbol{r};\omega)\right] = 0. \tag{1.1.67}$$

Equations (1.1.64) and (1.1.65) are the so-called *Stratton-Chu formulas* [9] which, similarly to the (1.1.48) for scalar fields, have two integrals: the first one dealing with the direct computation of the fields from sources distributions, the second one to formulate the vector Huygen's principle.

It is to be noted that, for the fields extinction out of V and for the continuity equations of the fields (1.1.28-1.1.30)[8], the terms $\hat{\boldsymbol{n}}\times\tilde{\boldsymbol{E}}(\boldsymbol{r}';\omega)$, $\hat{\boldsymbol{n}}\times\tilde{\boldsymbol{H}}(\boldsymbol{r}';\omega)$, $\hat{\boldsymbol{n}}\cdot\tilde{\boldsymbol{E}}(\boldsymbol{r}';\omega)$ and $\hat{\boldsymbol{n}}\cdot\tilde{\boldsymbol{H}}(\boldsymbol{r}';\omega)$ in the second integrands of (1.1.64) and (1.1.65) correspond to, respectively, the surface currents $-\vec{\boldsymbol{J}}_{ms}(\boldsymbol{r},\omega)$ and $\tilde{\boldsymbol{J}}_s(\boldsymbol{r},\omega)$, and surface charges related terms $1/\epsilon\,\tilde{\rho}_s(\boldsymbol{r},\omega)$ and $1/\mu\,\tilde{\rho}_{ms}(\boldsymbol{r},\omega)$, all of them located on S_0. These surface sources are also named *equivalent sources* as they take place to represent the equivalent unbounded electromagnetic problem.

For a practical use of the Stratton-Chu formulas (1.1.64-1.1.65), it is interesting to convert them into a form that does not contain charge densities sources and equivalent surface charge densities. This is achieved with the use of the continuity equations (1.1.19) and (1.1.26). We begin for the electric field, recasting the second integrand term of the first integral of (1.1.64) in the following manner:

$$\begin{aligned}\int_V \frac{1}{\epsilon}\tilde{\rho}\nabla' G\,dV' &= -\frac{1}{j\omega\epsilon}\int_V (\nabla'\cdot\tilde{\boldsymbol{J}})\nabla' G\,dV' \\ &= -\frac{1}{j\omega\epsilon}\left[\int_V \nabla'\cdot(\tilde{\boldsymbol{J}}\nabla' G)\,dV' - \right. \\ &\qquad \left.\int_V (\tilde{\boldsymbol{J}}\cdot\nabla')\nabla' G\,dV'\right],\end{aligned} \tag{1.1.68}$$

where the vector identity [7]

$$\nabla\cdot(\boldsymbol{\Omega}\boldsymbol{\Psi}) = (\nabla\cdot\boldsymbol{\Omega})\boldsymbol{\Psi}+\boldsymbol{\Omega}\cdot(\nabla\boldsymbol{\Psi}) = (\nabla\cdot\boldsymbol{\Omega})\boldsymbol{\Psi}+(\boldsymbol{\Omega}\cdot\nabla)\boldsymbol{\Psi} \tag{1.1.69}$$

have been employed with $\boldsymbol{\Psi}=\nabla G$ and $\boldsymbol{\Omega}=\tilde{\boldsymbol{J}}$. The first integral in right-hand side of (1.1.68), for the divergence theorem (1.1.41), becomes

$$-\frac{1}{j\omega\epsilon}\int_V \nabla\cdot(\tilde{\boldsymbol{J}}\nabla G)\,dV' = \frac{1}{j\omega\epsilon}\oint_S (\tilde{\boldsymbol{J}}\nabla G)\cdot\hat{\boldsymbol{n}}\,dS', \tag{1.1.70}$$

[8] $\tilde{\boldsymbol{E}}_2(\boldsymbol{r}';\omega)=\tilde{\boldsymbol{H}}_2(\boldsymbol{r}';\omega)=0$, $\tilde{\boldsymbol{E}}(\boldsymbol{r}';\omega)=\tilde{\boldsymbol{H}}_1(\boldsymbol{r}';\omega)$, $\tilde{\boldsymbol{H}}(\boldsymbol{r}';\omega)=\tilde{\boldsymbol{H}}_1(\boldsymbol{r}';\omega)$ and $\hat{\boldsymbol{n}}$ inwardly directed to V (region 1).

which vanishes if the volume V surrounded by S is chosen such that it slightly exceed that needed to contain the impressed sources. We obtain

$$\int_V \frac{1}{\epsilon}\tilde{\rho}\nabla G\, dV' = \frac{1}{j\omega\epsilon}\int_V (\tilde{\boldsymbol{J}}\cdot\nabla)\nabla G\, dV'. \tag{1.1.71}$$

Assuming now the charge and current densities of (1.1.71) to be located on the surface S_0 (to be of surface kind) and using the continuity equations (1.1.28-1.1.30), we can write

$$\int_V [j\omega\tilde{\rho}_s - (\tilde{\boldsymbol{J}}_s\cdot\nabla')]\nabla' G\, dV' = 0 = \oint_{S_0} [j\omega\epsilon(\hat{\boldsymbol{n}}\cdot\tilde{\boldsymbol{E}}) - ((\hat{\boldsymbol{n}}\times\tilde{\boldsymbol{H}})\cdot\nabla')]\nabla' G\, dS'. \tag{1.1.72}$$

Thus, the Stratton-Chu equation for the electric field (1.1.64) can be rewritten into the following *Kottler's form* [8]

$$\tilde{\boldsymbol{E}}(\boldsymbol{r};\omega) = \frac{1}{j\omega\epsilon}\int_V \left[k^2 G\tilde{\boldsymbol{J}} + (\tilde{\boldsymbol{J}}\cdot\nabla')\nabla' G - j\omega\epsilon\tilde{\boldsymbol{J}}_m\times\nabla' G\right] dV' + \frac{1}{j\omega\epsilon}\oint_{S_0}\left[k^2 G(\hat{\boldsymbol{n}}\times\tilde{\boldsymbol{H}}) + ((\hat{\boldsymbol{n}}\times\tilde{\boldsymbol{H}})\cdot\nabla')\nabla' G + j\omega\epsilon(\hat{\boldsymbol{n}}\times\tilde{\boldsymbol{E}})\times\nabla' G\right] dS'. \tag{1.1.73}$$

Analogously for the magnetic field, (1.1.65) becomes

$$\tilde{\boldsymbol{H}}(\boldsymbol{r};\omega) = \frac{1}{j\omega\mu}\int_V \left[k^2 G\tilde{\boldsymbol{J}}_m + (\tilde{\boldsymbol{J}}_m\cdot\nabla')\nabla' G + j\omega\mu\tilde{\boldsymbol{J}}\times\nabla' G\right] dV' + \frac{1}{j\omega\mu}\oint_{S_0}\left[-k^2 G(\hat{\boldsymbol{n}}\times\tilde{\boldsymbol{E}}) - ((\hat{\boldsymbol{n}}\times\tilde{\boldsymbol{E}})\cdot\nabla')\nabla' G + j\omega\mu(\hat{\boldsymbol{n}}\times\tilde{\boldsymbol{H}})\times\nabla' G\right] dS' \tag{1.1.74}$$

The surface integrals of Kotter's equations (1.1.73-1.1.74) state the so-called *Love's equivalence principle* [7] while considering the *equivalent electric and magnetic currents* $\tilde{\boldsymbol{J}}_s^{eq} = \hat{\boldsymbol{n}}\times\tilde{\boldsymbol{H}}$ and $\tilde{\boldsymbol{J}}_{ms}^{eq} = -\hat{\boldsymbol{n}}\times\tilde{\boldsymbol{E}}$ on the bounding surface S_0.

1.2 Scalar fields near-to-far transformations

In this section, we present a numerical implementation of the scalar fields near-to-far transformations (scalar N2F), relying on the mathematical formulation discussed in section 1.1.3. We first recall in a generic form the steps to be followed for

the scalar N2F, then a computation will be performed in Matlab[9] environment considering as enclosing surface firstly a sphere then a parallelepiped. The results will be compared to the direct computation of the far fields, assuming an unbounded medium.

1.2.1 Computation steps

For the computation of the near-zone or *Fresnel-zone* fields, we need to consider the sources distributed within the volume $V_{S_C} \subset V$, determined by the arbitrary surface S_C, chosen to be relatively close[10] to the sources. We also consider the surface S_0 going to zero, such that the second integral term in the right-hand side of equation (1.1.48) vanishes. We obtain:

$$\tilde{\psi}(\boldsymbol{r};\omega)\Big|_{S_C} = \int_{V_{S_C}} G(\boldsymbol{r}|\boldsymbol{r}';\omega)\,\tilde{S}(\boldsymbol{r}',\omega)\,dV' \tag{1.2.75}$$

where $\boldsymbol{r}'$ is a vector pointing to an infinitesimal source element. The problem's geometry is depicted in figure 1.3. The Green's function that will be used is the well-known *Green's function for free space*

$$G(\boldsymbol{r}|\boldsymbol{r}';\omega) = \frac{\mathrm{e}^{-jk|\boldsymbol{r}-\boldsymbol{r}'|}}{4\pi|\boldsymbol{r}-\boldsymbol{r}'|} \tag{1.2.76}$$

and the sources will be assumed to be radiating isotropically such that the whole radiating structure emits a unit of power, that is $\sum_{n=1}^{N} |\tilde{S}_n(\boldsymbol{r}',\omega)|^2 = 1$, with N the number of sources.

The computation of the far-zone or *Fraunhofer-zone* fields can be performed by simply setting the modulus of the vectors $\boldsymbol{r}$ of a consistent number of wavelengths (see note 10). This is the direct computation of the far fields from an arbitrary sources distribution. However, we are interested in the computation of the far fields not directly from the sources but from the near fields they produce. Looking at the equation

[9] Matlab© Mathworks. Further informations available on `www.mathworks.com`.

[10] The distance $\frac{2\,L^2}{\lambda}$, where L is the highest length in a planar distribution of point sources and λ the wavelength, is the distance from the sources where we commit a maximum phase error of $\pi/8$ in the plane wave approximation directed perpendicularly to the point sources distribution. This distance can be taken as a reference for the near-zone to far-zone fields transition and the near fields are typically considered to lie within $d \ll \frac{2\,L^2}{\lambda}$.

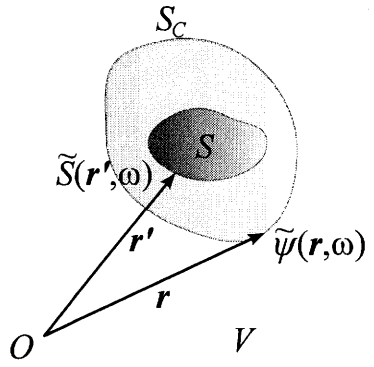

Figure 1.3: Near fields computations.

(1.1.48), we see that we can achieve this by letting S_0 be wide enough to encompass all the sources, such that they are not anymore part of V and the first integral term in the right-hand side of (1.1.48) goes to zero. Then, from the fields $\tilde{\psi}(\boldsymbol{r}';\omega)$ computed over S_0, we solve the second integral term to obtain the fields $\tilde{\psi}(\boldsymbol{r};\omega)$ $\forall \boldsymbol{r} \in V$. To make sure that the fields previously calculated with equation (1.2.75) equals $\tilde{\psi}(\boldsymbol{r}';\omega)$, we choose S_0 equal to S_C. Now, the equation to solve is

$$\tilde{\psi}(\boldsymbol{r};\omega) = \oint_{S_0=S_C} \left[\tilde{\psi}(\boldsymbol{r}';\omega) \frac{\partial G(\boldsymbol{r}|\boldsymbol{r}';\omega)}{\partial n'} - G(\boldsymbol{r}|\boldsymbol{r}';\omega) \frac{\partial \tilde{\psi}(\boldsymbol{r}';\omega)}{\partial n'} \right] dS'. \quad (1.2.77)$$

The scalar N2F step is depicted in figure 1.4.

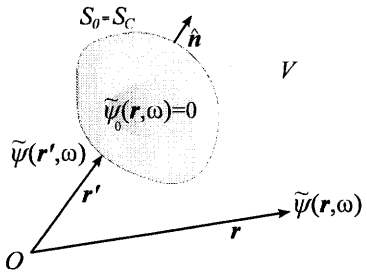

Figure 1.4: Near-to-far fields transformations.

1.2.2 Computations on a bounding sphere

Let us now assume the bounding surface $S_0 = S_C$ to be a sphere, and the origin of the reference system O to be located at the center of the sphere. The geometry of the

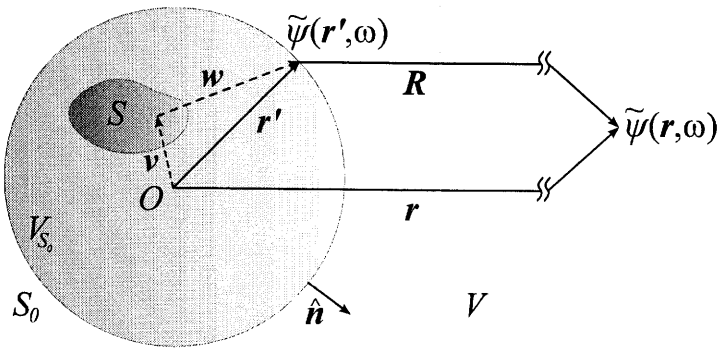

Figure 1.5: Near field to far field transformation from a bounding sphere.

problem is depicted in figure 1.5. The volume V is the entire free space excluded V_{S_0} which contains all the sources. The spherical geometry of the problem allows us to use spherical coordinates solving the previous equations (1.2.75) and (1.2.77).

The near fields are computed using the (1.2.75) for the given geometry and we have

$$\tilde{\psi}(\boldsymbol{r}';\omega)\Big|_{S_0} = \int_{V_{S_0}} \frac{\mathrm{e}^{-jk|\boldsymbol{r}'-\boldsymbol{v}|}}{4\pi|\boldsymbol{r}'-\boldsymbol{v}|}\,\tilde{S}(\boldsymbol{v},\omega)\,dV_{\boldsymbol{v}}. \tag{1.2.78}$$

Equation (1.2.78) gives the value of the near field surface density on a single infinitesimal point of the sphere indicated by $\boldsymbol{r}'$ (i.e. determined by the Green's function) and produced by the enclosed sources distribution.

We now proceed with the scalar N2F, provided that $\tilde{\psi}(\boldsymbol{r}';\omega)$ and its gradient $\nabla'\tilde{\psi}(\boldsymbol{r}';\omega)$ are known on the entire sphere.

Using $\frac{\mathrm{e}^{-jk|\boldsymbol{R}|}}{4\pi|\boldsymbol{R}|} = \frac{\mathrm{e}^{-jk|\boldsymbol{r}-\boldsymbol{r}'|}}{4\pi|\boldsymbol{r}-\boldsymbol{r}'|}$ as Green's function, the far fields become the following

$$\tilde{\psi}(\boldsymbol{r};\omega) = \oint_{S_0} \left[\tilde{\psi}(\boldsymbol{r}';\omega)\frac{\partial}{\partial n'}\frac{\mathrm{e}^{-jk|\boldsymbol{R}|}}{4\pi|\boldsymbol{R}|} - \frac{\mathrm{e}^{-jk|\boldsymbol{R}|}}{4\pi|\boldsymbol{R}|}\frac{\partial\tilde{\psi}(\boldsymbol{r}';\omega)}{\partial n'}\right] dS'. \tag{1.2.79}$$

The gradient of the Green's function is

$$\nabla_{\boldsymbol{R}}\frac{\mathrm{e}^{-jk|\boldsymbol{R}|}}{4\pi|\boldsymbol{R}|} = -\left(jk+\frac{1}{|\boldsymbol{R}|}\right)\frac{\mathrm{e}^{-jk|\boldsymbol{R}|}}{4\pi|\boldsymbol{R}|}\frac{\boldsymbol{R}}{|\boldsymbol{R}|} \tag{1.2.80}$$

and the integrand term of (1.2.79)

$$\begin{aligned}\frac{\partial}{\partial n'}\frac{\mathrm{e}^{-jk|\boldsymbol{R}|}}{4\pi|\boldsymbol{R}|} &= \hat{\boldsymbol{n}}\cdot\nabla'\frac{\mathrm{e}^{-jk|\boldsymbol{r}-\boldsymbol{r}'|}}{4\pi|\boldsymbol{r}-\boldsymbol{r}'|} = -\hat{\boldsymbol{n}}\cdot\nabla\frac{\mathrm{e}^{-jk|\boldsymbol{r}-\boldsymbol{r}'|}}{4\pi|\boldsymbol{r}-\boldsymbol{r}'|} = -\hat{\boldsymbol{n}}\cdot\nabla_{\boldsymbol{R}}\frac{\mathrm{e}^{-jk|\boldsymbol{R}|}}{4\pi|\boldsymbol{R}|} \\ &= \left(jk+\frac{1}{|\boldsymbol{R}|}\right)\frac{\mathrm{e}^{-jk|\boldsymbol{R}|}}{4\pi|\boldsymbol{R}|}\left(\frac{\boldsymbol{R}}{|\boldsymbol{R}|}\cdot\hat{\boldsymbol{n}}\right).\end{aligned} \tag{1.2.81}$$

For the spherical shape of the surface S_0, its normal inwardly directed to V, is $\hat{\boldsymbol{n}} = \frac{\boldsymbol{r}'}{|\boldsymbol{r}'|}$ and equation (1.2.79) can be rewritten as follows

$$\begin{aligned}
\tilde{\psi}(\boldsymbol{r};\omega) &= \oint_{S_0} \left[\tilde{\psi}(\boldsymbol{r}';\omega)\left(jk+\frac{1}{|\boldsymbol{R}|}\right)\frac{\mathrm{e}^{-jk|\boldsymbol{R}|}}{4\pi|\boldsymbol{R}|}\left(\frac{\boldsymbol{R}}{|\boldsymbol{R}|}\cdot\frac{\boldsymbol{r}'}{|\boldsymbol{r}'|}\right) - \frac{\mathrm{e}^{-jk|\boldsymbol{R}|}}{4\pi|\boldsymbol{R}|}\frac{\partial\tilde{\psi}(\boldsymbol{r}';\omega)}{\partial n'}\right] dS' \\
&= \oint_{S_0} \frac{\mathrm{e}^{-jk|\boldsymbol{R}|}}{4\pi|\boldsymbol{R}|}\left[\left(jk+\frac{1}{|\boldsymbol{R}|}\right)\tilde{\psi}(\boldsymbol{r}';\omega)\left(\frac{\boldsymbol{R}}{|\boldsymbol{R}|}\cdot\frac{\boldsymbol{r}'}{|\boldsymbol{r}'|}\right) - \frac{\partial\tilde{\psi}(\boldsymbol{r}';\omega)}{\partial n'}\right] dS' \\
&= \oint_{S_0} \frac{\mathrm{e}^{-jk|\boldsymbol{R}|}}{4\pi|\boldsymbol{R}|}\left[\left(jk+\frac{1}{|\boldsymbol{R}|}\right)\tilde{\psi}(\boldsymbol{r}';\omega)\left(\frac{\boldsymbol{R}}{|\boldsymbol{R}|}\cdot\frac{\boldsymbol{r}'}{|\boldsymbol{r}'|}\right) - \right. \\
&\qquad \left. \frac{\partial\tilde{\psi}(\boldsymbol{r}';\omega)}{\partial r'}\left(\frac{\boldsymbol{r}'}{|\boldsymbol{r}'|}\cdot\frac{\boldsymbol{r}'}{|\boldsymbol{r}'|}\right)\right] dS' \\
&= \oint_{S_0} \frac{\mathrm{e}^{-jk|\boldsymbol{R}|}}{4\pi|\boldsymbol{R}|}\left[\left(jk+\frac{1}{|\boldsymbol{R}|}\right)\tilde{\psi}(\boldsymbol{r}';\omega)\left(\frac{\boldsymbol{R}}{|\boldsymbol{R}|}\cdot\frac{\boldsymbol{r}'}{|\boldsymbol{r}'|}\right) - \frac{\partial\tilde{\psi}(\boldsymbol{r}';\omega)}{\partial r'}\right] dS'. \qquad (1.2.82)
\end{aligned}$$

where we have used the identity $\frac{\partial}{\partial n'} = \left(\frac{\boldsymbol{r}'}{|\boldsymbol{r}'|}\cdot\hat{\boldsymbol{n}}\right)\frac{\partial}{\partial r'}$.

As we are only interested in the far-zone fields, we can make the following approximations for $|\boldsymbol{R}|$ noting that

$$R = \sqrt{(\boldsymbol{r}-\boldsymbol{r}')\cdot(\boldsymbol{r}-\boldsymbol{r}')} = \sqrt{r^2 - 2(\boldsymbol{r}\cdot\boldsymbol{r}') + r'^2}, \qquad (1.2.83)$$

such that for $\boldsymbol{R}$ in the far-zone we have $r \gg r'$, hence $\frac{\boldsymbol{R}}{|\boldsymbol{R}|} = \hat{\boldsymbol{R}} \approx \hat{\boldsymbol{r}}$ and the dominant terms of a Taylor expansion for the square root gives

$$R = r\sqrt{1 - 2\frac{(\hat{\boldsymbol{r}}\cdot\boldsymbol{r}')}{r} + \left(\frac{r'}{r}\right)^2} \approx r\left[1 - \frac{(\hat{\boldsymbol{r}}\cdot\boldsymbol{r}')}{r}\right] = r - \hat{\boldsymbol{r}}\cdot\boldsymbol{r}'. \qquad (1.2.84)$$

Thus, the Green's function may be approximated as

$$G(\boldsymbol{r}|\boldsymbol{r}';\omega) = \frac{\mathrm{e}^{-jk|\boldsymbol{R}|}}{4\pi|\boldsymbol{R}|} \approx \frac{\mathrm{e}^{-jkr}}{4\pi r}\mathrm{e}^{jk\hat{\boldsymbol{r}}\cdot\boldsymbol{r}'}. \qquad (1.2.85)$$

The equation (1.2.82) becomes

$$\begin{aligned}
\tilde{\psi}(\boldsymbol{r};\omega)\Big|_{r\gg r'} &\approx \oint_{S_0} \frac{\mathrm{e}^{-jkr}}{4\pi r}\mathrm{e}^{jk\hat{\boldsymbol{r}}\cdot\boldsymbol{r}'}\left[\left(jk+\frac{1}{r}\right)\tilde{\psi}(\boldsymbol{r}';\omega)(\hat{\boldsymbol{r}}\cdot\hat{\boldsymbol{r}}') - \frac{\partial\tilde{\psi}(\boldsymbol{r}';\omega)}{\partial r'}\right] dS' \\
&\approx \frac{\mathrm{e}^{-jkr}}{4\pi r}\oint_{S_0} \mathrm{e}^{jk\hat{\boldsymbol{r}}\cdot\boldsymbol{r}'}\left[\left(jk+\frac{1}{r}\right)\tilde{\psi}(\boldsymbol{r}';\omega)(\hat{\boldsymbol{r}}\cdot\hat{\boldsymbol{r}}') - \frac{\partial\tilde{\psi}(\boldsymbol{r}';\omega)}{\partial r'}\right] dS' \\
&\underset{kr\gg 1}{\approx} \frac{\mathrm{e}^{-jkr}}{4\pi r}\oint_{S_0} \mathrm{e}^{jk\hat{\boldsymbol{r}}\cdot\boldsymbol{r}'}\left[jk\tilde{\psi}(\boldsymbol{r}';\omega)(\hat{\boldsymbol{r}}\cdot\hat{\boldsymbol{r}}') - \frac{\partial\tilde{\psi}(\boldsymbol{r}';\omega)}{\partial r'}\right] dS'. \qquad (1.2.86)
\end{aligned}$$

Finally, the radiation pattern is computed from (1.2.86), removing the distance r dependence by the following limit

$$\begin{aligned}\mathscr{P}(\hat{\boldsymbol{r}};\omega) &= \lim_{r\to\infty} 4\pi r^2 \left|\tilde{\psi}(\boldsymbol{r};\omega)\right|^2 \\ &= \left|\oint_{S_0} \mathrm{e}^{jk\hat{\boldsymbol{r}}\cdot\boldsymbol{r}'}\left[jk\tilde{\psi}(\boldsymbol{r}';\omega)(\hat{\boldsymbol{r}}\cdot\hat{\boldsymbol{r}}') - \frac{\partial\tilde{\psi}(\boldsymbol{r}';\omega)}{\partial r'}\right] dS'\right|^2 \\ &= \left|\tilde{\psi}_r^*\right|^2, \end{aligned} \tag{1.2.87}$$

where $\tilde{\psi}_r^* \in \mathbb{C}$ is the *far field detector.*

1.2.2.1 Pattern in spherical coordinates

Because of the spherical symmetry of the N2F problem of the sphere, it is interesting to express the vectors $\boldsymbol{r}$ and $\boldsymbol{r}'$ with spherical variables for the solution of equation (1.2.87). To evaluate the scalar products, we can rely on Cartesian unit vectors basis with the components of the vectors are dependent on spherical variables. The unit vectors involved in the far fields detectors are, respectively,

$$\begin{aligned}\hat{\boldsymbol{r}}' &= \cos(\theta_{r'})\cos(\phi_{r'})\,\hat{\boldsymbol{i}}_x + \cos(\theta_{r'})\sin(\phi_{r'})\,\hat{\boldsymbol{i}}_y + \sin(\theta_{r'})\,\hat{\boldsymbol{i}}_z, \\ \hat{\boldsymbol{r}} &= \cos(\theta_r)\cos(\phi_r)\,\hat{\boldsymbol{i}}_x + \cos(\theta_r)\sin(\phi_r)\,\hat{\boldsymbol{i}}_y + \sin(\theta_r)\,\hat{\boldsymbol{i}}_z, \end{aligned} \tag{1.2.88}$$

and their scalar product is given by

$$\begin{aligned}\xi(\theta_r,\phi_r,\theta_{r'},\phi_{r'}) &= \cos(\theta_r)\cos(\phi_r)\cos(\theta_{r'})\cos(\phi_{r'}) + \\ &\quad \cos(\theta_r)\sin(\phi_r)\cos(\theta_{r'})\sin(\phi_{r'}) + \\ &\quad \sin(\theta_r)\sin(\theta_{r'}) \\ &= \sin(\theta_r)\sin(\theta_{r'})\cos(\phi_r-\phi_{r'}) + \\ &\quad \cos(\theta_r)\cos(\theta_{r'}). \end{aligned} \tag{1.2.89}$$

The equation (1.2.87) can be written as follows

$$\mathscr{P}(\theta_r,\phi_r;\omega) = \left|\int_0^{2\pi}\int_0^{\pi} \mathrm{e}^{jkr'\xi'}\left[jk\tilde{\psi}'_{r'}\xi' - \frac{\partial\tilde{\psi}'_{r'}}{\partial r'}\right] r'^2\sin(\theta_{r'})\,d\theta_{r'}\,d\phi_{r'}\right|^2 \tag{1.2.90}$$

where $\tilde{\psi}'_{r'} = \tilde{\psi}(r',\theta_{r'},\phi_{r'};\omega)$ and $\xi' = \xi(\theta_r,\phi_r,\theta_{r'},\phi_{r'})$.

1.2.2.2 Numerical implementation

Here follow the results obtained from a Matlab implementation that computes the pattern from planar array of 3 by 5 point sources ($N = 15$ point sources), the firsts on the x direction and the latter along y. The point sources or array elements are chosen to be equally spaced of $\lambda/2$. Due to power normalization, the maximum gain or *directivity* the array can achieve equals the total number of point sources, that is $10\log_{10}(N) \approx 11.76$ dB [4].

From (1.2.86), we can see that the values we have to compute in the first step are the near fields $\tilde{\psi}(\boldsymbol{r}';\omega)$ and their radial derivatives $\frac{\partial\tilde{\psi}(\boldsymbol{r}';\omega)}{\partial r'}$. The firsts are achieved by the numerical integration of the volume integral (1.2.78), considering $\tilde{S}(\boldsymbol{v}_n,\omega) = \tilde{S}_n\delta(\boldsymbol{v}-\boldsymbol{v}_n), n = 1\ldots N$. We obtain

$$\tilde{\psi}_m(\boldsymbol{r'}_m;\omega) = \sum_{n=1}^{N}\frac{\mathrm{e}^{-jk|\boldsymbol{r'}_m-\boldsymbol{v}_n|}}{4\pi|\boldsymbol{r'}_m-\boldsymbol{v}_n|}\tilde{S}_n \qquad n=1\ldots N,\ m=1\ldots M \quad (1.2.91)$$

where we have discretized the sphere in M sampling points. The second ones, noting that $\tilde{S}(\boldsymbol{v},\omega)$ has no dependence on the vector $\boldsymbol{r}'$, can be evaluated proceeding in the following manner

$$\begin{aligned}\frac{\partial\tilde{\psi}(\boldsymbol{r}';\omega)}{\partial r'} &= \frac{\partial}{\partial r'}\int_{V_{S_0}}\frac{\mathrm{e}^{-jk|\boldsymbol{r}'-\boldsymbol{v}|}}{4\pi|\boldsymbol{r}'-\boldsymbol{v}|}\tilde{S}(\boldsymbol{v},\omega)dV_v \\ &= \int_{V_{S_0}}\frac{\partial}{\partial r'}\frac{\mathrm{e}^{-jk|\boldsymbol{r}'-\boldsymbol{v}|}}{4\pi|\boldsymbol{r}'-\boldsymbol{v}|}\tilde{S}(\boldsymbol{v},\omega)dV_v \qquad \forall\boldsymbol{r}'\neq\boldsymbol{v} \\ &= -\int_{V_{S_0}}\left(jk+\frac{1}{|\boldsymbol{r}'-\boldsymbol{v}|}\right)\frac{\mathrm{e}^{-jk|\boldsymbol{r}'-\boldsymbol{v}|}}{4\pi|\boldsymbol{r}'-\boldsymbol{v}|}\left(\frac{\boldsymbol{r}'-\boldsymbol{v}}{|\boldsymbol{r}'-\boldsymbol{v}|}\cdot\hat{\boldsymbol{r}}'\right)\tilde{S}(\boldsymbol{v},\omega)dV_v \quad (1.2.92)\end{aligned}$$

which becomes, in a numerical form,

$$\begin{aligned}\frac{\partial\tilde{\psi}_m(\boldsymbol{r'}_m;\omega)}{\partial r'_m} &= -\sum_{n=1}^{N}\left(jk+\frac{1}{|\boldsymbol{r'}_m-\boldsymbol{v}_n|}\right)\frac{\mathrm{e}^{-jk|\boldsymbol{r'}_m-\boldsymbol{v}_n|}}{4\pi|\boldsymbol{r'}_m-\boldsymbol{v}_n|}\left(\frac{\boldsymbol{r'}_m-\boldsymbol{v}_n}{|\boldsymbol{r'}_m-\boldsymbol{v}_n|}\cdot\hat{\boldsymbol{r}}'_m\right)\tilde{S}_n \\ &\qquad n=1\ldots N,\ m=1\ldots M. \quad (1.2.93)\end{aligned}$$

The near-to-far transformation from a bounding sphere, varying the sampling resolution in terms of wavelengths and using a *midpoint*[11] *numerical integration* of

[11] The fields sampling points are located in the middle of surface patches dS_n, and an integration of a discretized function Φ_n is obtained by the sum $\sum_{n=1}^{N}\Phi_n dS_n$. The *Trapezoidal rule* have also been tested, with no significant improvement in the pattern error. Further enhancements can be achieved with *Gaussian quadrature.* [12]

(1.2.87) over the sphere, will be compared to the direct computation of the pattern. We obtain the N2F numerical formula

$$\mathscr{P}_{p\mathrm{N2F}}\left(\hat{\boldsymbol{r}}_p;\omega\right) = \left|\tilde{\psi}^*_{r_p}\right|^2 = \left|\sum_{m=1}^{M} \mathrm{e}^{jk\hat{\boldsymbol{r}}_p\cdot\boldsymbol{r}'_m}\left[jk\tilde{\psi}_m(\boldsymbol{r}'_m;\omega)\left(\hat{\boldsymbol{r}}_p\cdot\hat{\boldsymbol{r}}'_m\right) - \frac{\partial\tilde{\psi}_m(\boldsymbol{r}'_m;\omega)}{\partial r'_m}\right] dS_m\right|^2. \quad m=1\ldots M,\ p=1\ldots P. \tag{1.2.94}$$

The direct field computation is derived from formula (1.2.91), with $\boldsymbol{r}'_m$ to become the far field vectors $\boldsymbol{r}_p$, assuming the far fields approximation (1.2.85) and applying the far-zone limit used in (1.2.87), that is

$$\begin{aligned}\mathscr{P}_{p\mathrm{Direct}}\left(\hat{\boldsymbol{r}}_p;\omega\right) &= \lim_{r_p\to\infty} 4\pi r_p^2\left|\frac{\mathrm{e}^{-jkr_p}}{4\pi r_p}\sum_{n=1}^{N}\mathrm{e}^{jk\hat{\boldsymbol{r}}_p\cdot\boldsymbol{v}_n}\,\tilde{S}_n\right|^2 \\ &= \left|\sum_{n=1}^{N}\mathrm{e}^{jk\hat{\boldsymbol{r}}_p\cdot\boldsymbol{v}_n}\,\tilde{S}_n\right|^2 \qquad n=1\ldots N,\ p=1\ldots P.\end{aligned} \tag{1.2.95}$$

The geometry of the discretized domain is depicted in figure 1.6. The radius of the sphere is set to be radially $\lambda/2$ away from the corner elements, i.e. $|\boldsymbol{r}'_m| = 1.618\lambda$ and the angles $\theta_{r'}$ and $\phi_{r'}$ of near field sampling are computed assuming $|\boldsymbol{r}'_m|\Delta\theta_{r'} \approx |\boldsymbol{r}'_m|\Delta\phi_{r'} \approx \lambda/10$.

Notice that the radial extension of the sphere from the array cannot be lower than the sampling resolution (inferior limit), and the superior limit is associated to the increasing memory consumption, in order to keep the desired resolution, as the sphere radius grows.

Figures 1.7 and 1.8 show the radiation patterns computed[12], respectively, in the $\phi_r = 0°$ (XZ) and $\phi_r = 90°$ (YZ) cut planes. The solid line corresponds to the N2F computed pattern while the crosses correspond to the direct pattern.

Let us discuss now on the error committed in the N2F computation, relatively to the direct one. In effect, the values of the gain in the two cases are slightly different, mainly due to the accuracy of the integration method used. Figure 1.9 shows the error

[12] Notice that the plotted patterns in 1.7 and 1.8 correspond to the *array factor*, the *element factor* being unitary in an array analysis. [2]

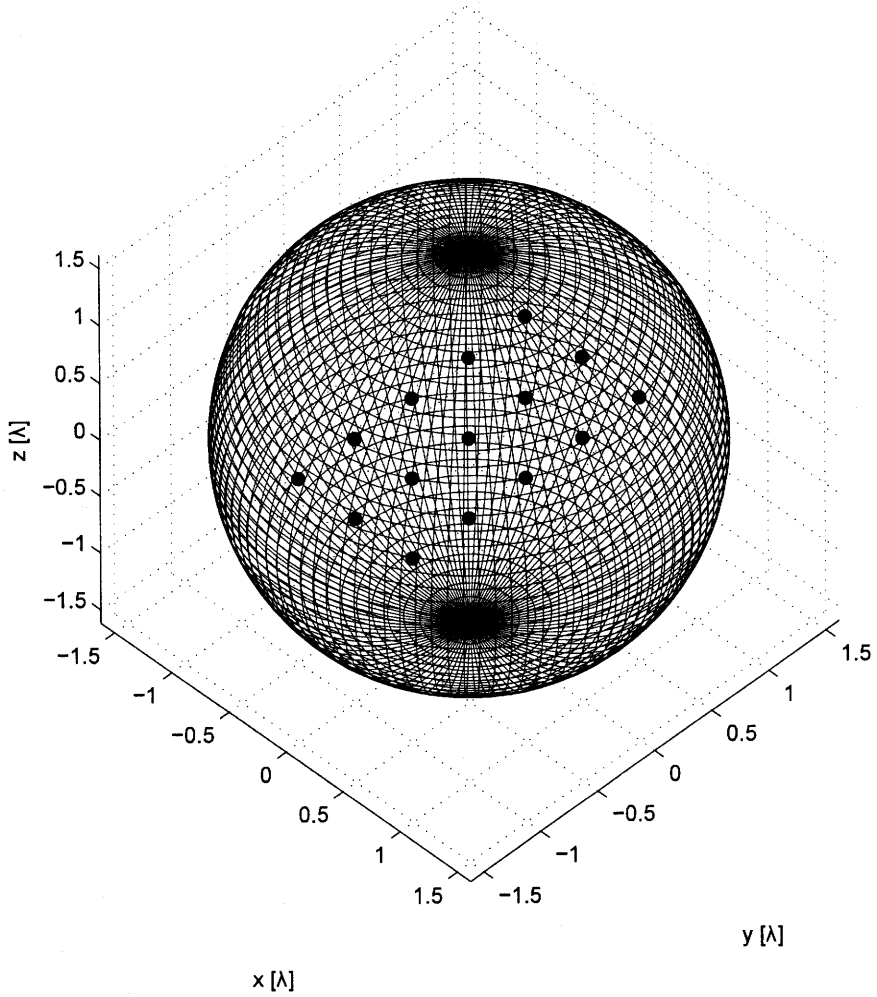

Figure 1.6: N2F bounding sphere and 3 by 5 point sources, with $\lambda/10$ sampling resolution. The samples are taken in the middle of the sphere patches.

in $\tilde{\psi}^*_{r\ \mathrm{N2F}}$ relatively to $\tilde{\psi}^*_{r\ \mathrm{Direct}}$ in the $\mathbb{L}_1$, $\mathbb{L}_2$ and $\mathbb{L}_\infty$ norms [17] for different resolutions, starting from $\lambda/2$ and progressively halving the resolution. We have chosen the $\mathbb{L}^2$ norm or *Euclidean norm* to compare the values of $\tilde{\psi}^*_{r\ \mathrm{N2F}}$ and $\tilde{\psi}^*_{r\ \mathrm{Direct}}$. This is motivated by the fact that the $\mathbb{L}^2$ norm preserves energy information. Thus, the scalar N2F relative error will be given by the following relation[13]

$$\varepsilon_{[\lambda/n]} = \frac{\|\tilde{\psi}^*_{r\ \mathrm{Direct}} - \tilde{\psi}^*_{r\ \mathrm{N2F}}\|_2}{\|\tilde{\psi}^*_{r\ \mathrm{Direct}}\|_2} \qquad n \in \mathbb{N}^+/\{1\}. \tag{1.2.96}$$

As we can see in figures 1.7 and 1.8, the sampling resolution of $\lambda/10$ with an error

[13] For *Shannon's sampling theorem*, the lowest sampling resolution that can be used equals $\lambda/2$.

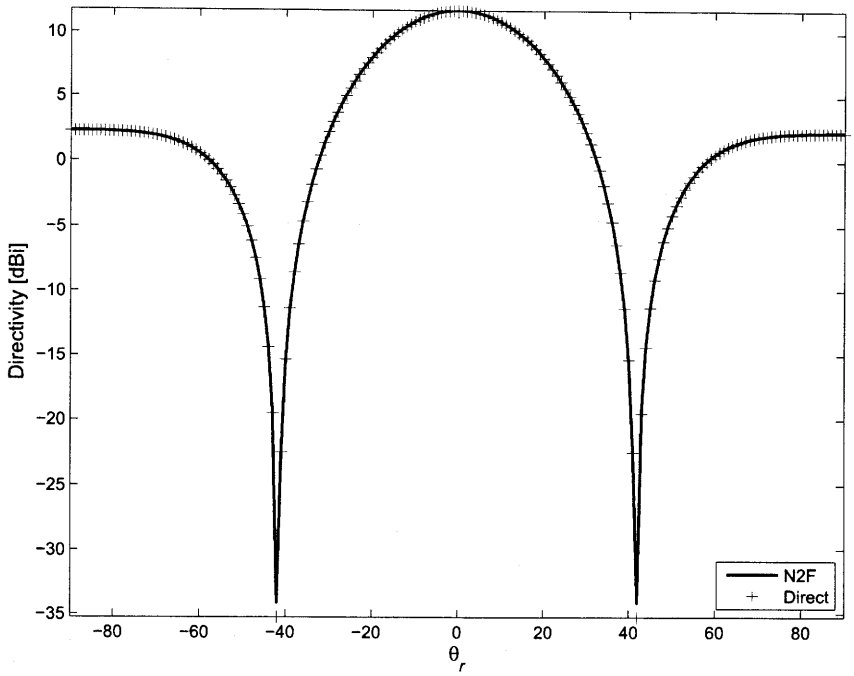

Figure 1.7: Pattern computed for equally phased point sources (broadside pattern) on the $\phi = 0°$ cut plane with $\lambda/10$ sampling resolution.

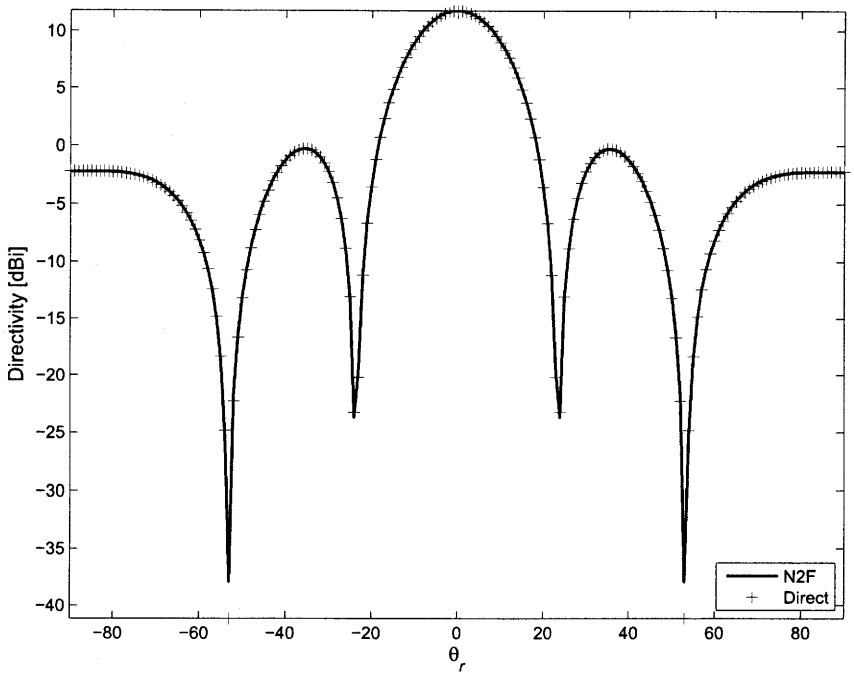

Figure 1.8: Pattern computed for equally phased point sources on the $\phi = 90°$ cut plane with $\lambda/10$ sampling resolution.

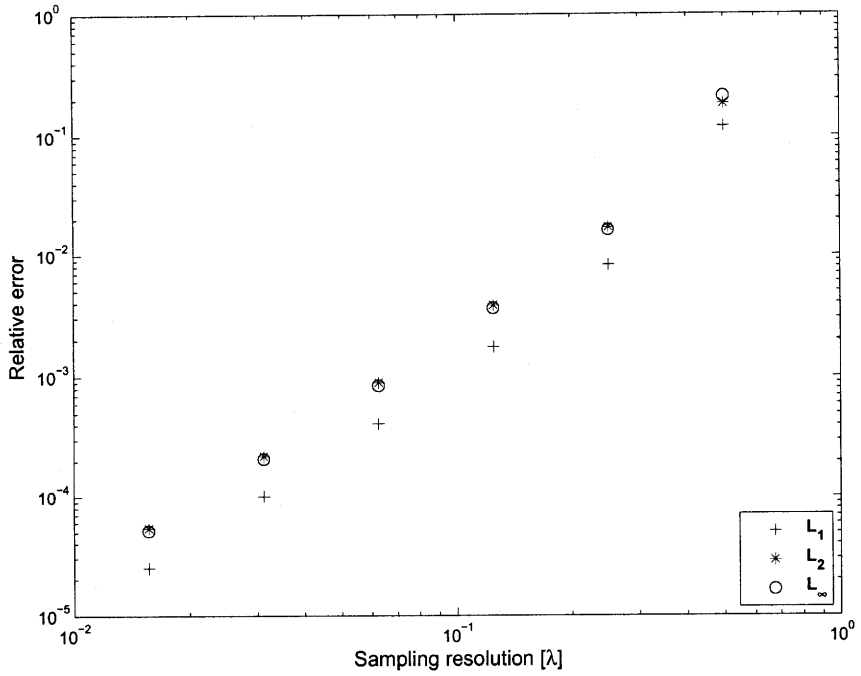

Figure 1.9: Relative broadside field detector $\tilde{\psi}_r^*$ error in the $\mathbb{L}_1$, $\mathbb{L}_2$ and $\mathbb{L}_\infty$ norms for several sampling resolutions.

of $\varepsilon_{[\lambda/10]} = 2.398\ 10^{-3}$ for 181 *look angles* ($\Delta\theta_r = 1°$), that is the far zone directions in which $\tilde{\psi}^*_{r\ \mathrm{N2F}}$ and $\tilde{\psi}^*_{r\ \mathrm{Direct}}$ are computed, provides a pattern that can be considered reasonably accurate. As we can see in figure 1.10, the number of look angles chosen does not significantly modify the error order even if the pattern is coarsely sampled (low number of look angles). However, there is a converging behavior while increasing the pattern sampling resolution ($\Delta\theta_r \to 0$). In order to define an accuracy criterion for the pattern computation, we will assume error values $\varepsilon_{[\lambda/n]} \leq 5\ 10^{-3}$ to be admissible, and the integer n will be consequently defined for the employed bounding surface. To motivate this choice, an example of pattern resulting in a higher error value ($\varepsilon_{[\lambda/3]} = 3.387\ 10^{-2}$) is given in figure 1.11, showing a sensible misfit comparing to the reference pattern (directly computed), especially in the side lobes.

Before we proceed with the N2F computations from a parallelepiped, let us face the steering operation, choosing opportunely the phase of $\tilde{S}_n, n = 1 \ldots N$, such that the main lobe in the pattern results in a desired direction. For a planar array with arbitrarily spaced sources, the phase values are $\phi_n = -k(x_n \sin(\theta_x) + y_n \sin(\theta_y))$

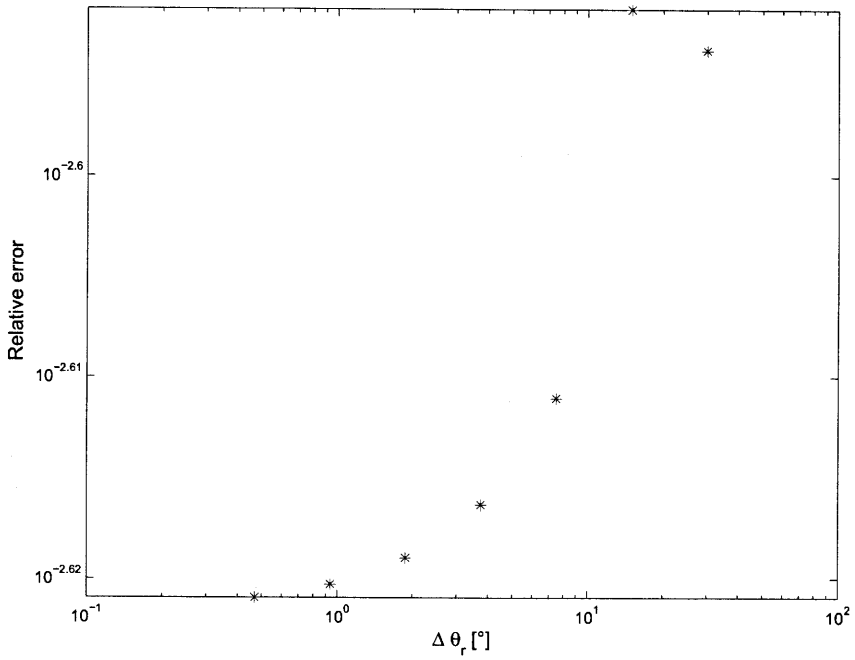

Figure 1.10: Relative broadside field detector pattern $\tilde{\psi}_r^*$ error in the $\mathbb{L}_2$ norm for several $\Delta\theta_r$, i.e. increasing the pattern resolution.

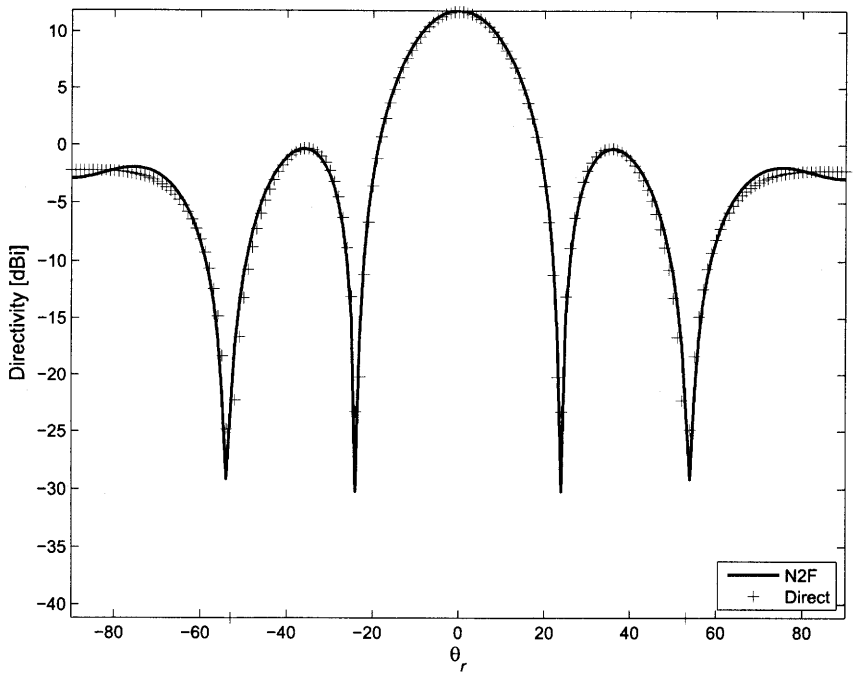

Figure 1.11: Pattern computed on the $\phi = 90°$ cut plane with $\lambda/3$ sampling resolution. Notice the visible error on the side lobes.

[2] where (x_n, y_n) are the position coordinates of the n^{th} source, θ_x and θ_y are, respectively, the *scan angles* along the x and y directions. Considering also the power normalization (see section 1.2.1), the sources phasors become

$$\tilde{S}_n = \frac{1}{\sqrt{N}} \, \mathrm{e}^{-jk(x_n \sin(\theta_x) + y_n \sin(\theta_y))} \qquad n = 1 \ldots N \tag{1.2.97}$$

Figures 1.12 and 1.13 show the patterns on the cut planes XZ and YZ resulting from the steering operation of $\theta_x = 10°$ and $\theta_y = 30°$.

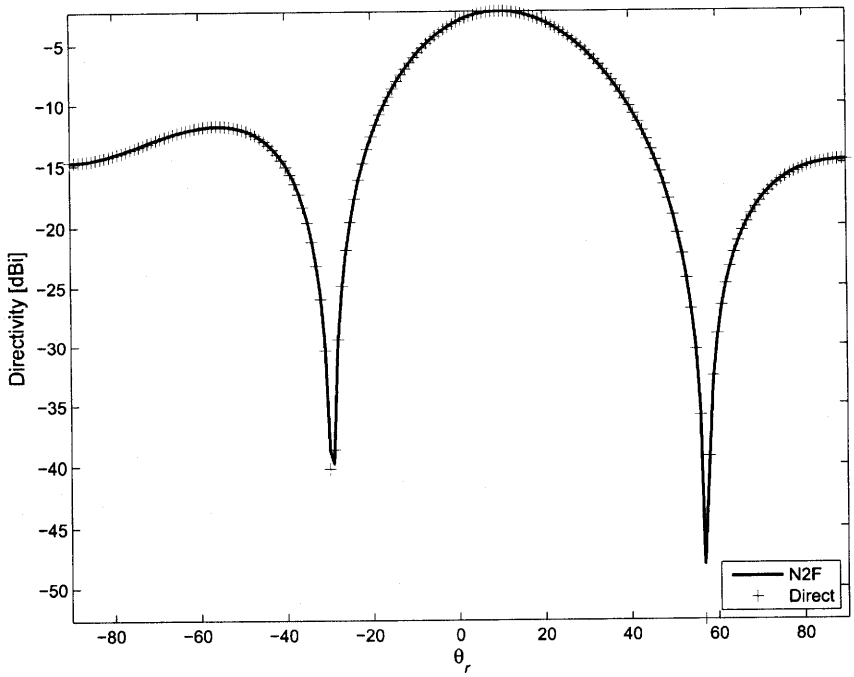

Figure 1.12: Pattern computed on the $\phi = 0°$ cut plane with $\lambda/10$ sampling resolution and scan angles $\theta_x = 10°$ and $\theta_y = 30°$.

1.2.3 Computations on a bounding parallelepiped

The N2F computation on a bounding parallelepiped or box is achieved similarly to the one from a bounding sphere. Figure 1.14 shows the mesh realized for the array of 3 by 5 point sources, with a resolution of $\lambda/10$. The minimum distance between a point source and a surface patch is of $\lambda/2$.

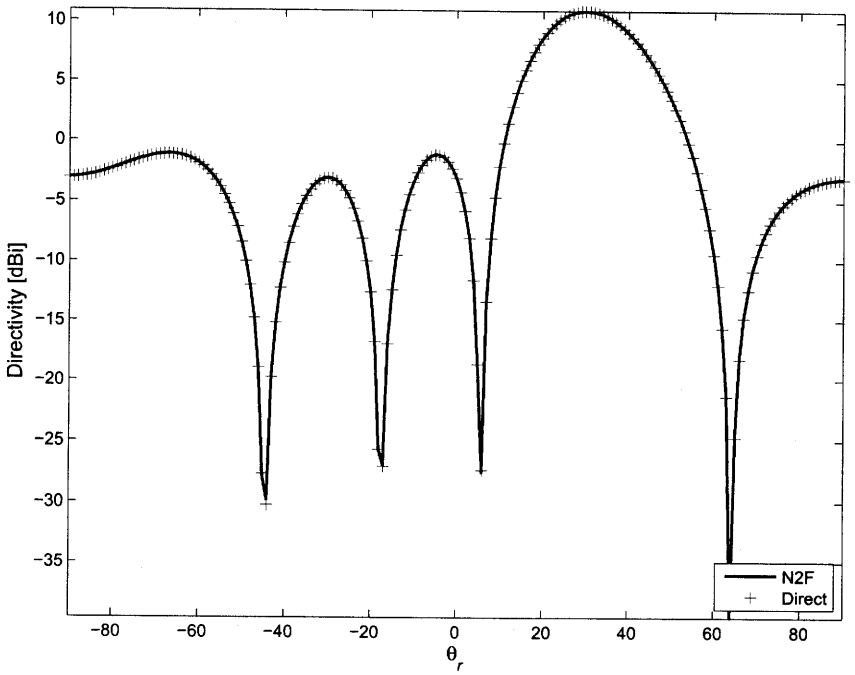

Figure 1.13: Pattern computed on the $\phi = 90°$ cut plane with $\lambda/10$ sampling resolution and scan angles $\theta_x = 10°$ and $\theta_y = 30°$.

The main difference between the two kinds of sampling geometries resides in the fact that the box requires a lower number of samples to achieve the same error as sphere's one. It is clear that as long as we get far away from the point sources, we need a higher number of near fields sampling points to keep the resolution desired. The box is in fact a closer encompassing surface. In figure 1.15 and table 1.1, it is shown the improvement we obtain using a bounding box. In the average and for the chosen array, the box needs about half of the sphere's number of sampling points, thus halving the memory requirements while keeping the same error level.

An interesting issue, seeking for further sampling coarsening to reduce the memory requirements, is to see what may happen if we omit some of the faces of the box, keeping the ones we expect to have higher power. The near fields sampled on the box in a broadside steering condition are plotted in figures 1.16 and 1.17.

We can see that the highest intensities are located on the top and bottom faces. To avoid significant disturbance in the remotion of the lateral faces, we prefer to further

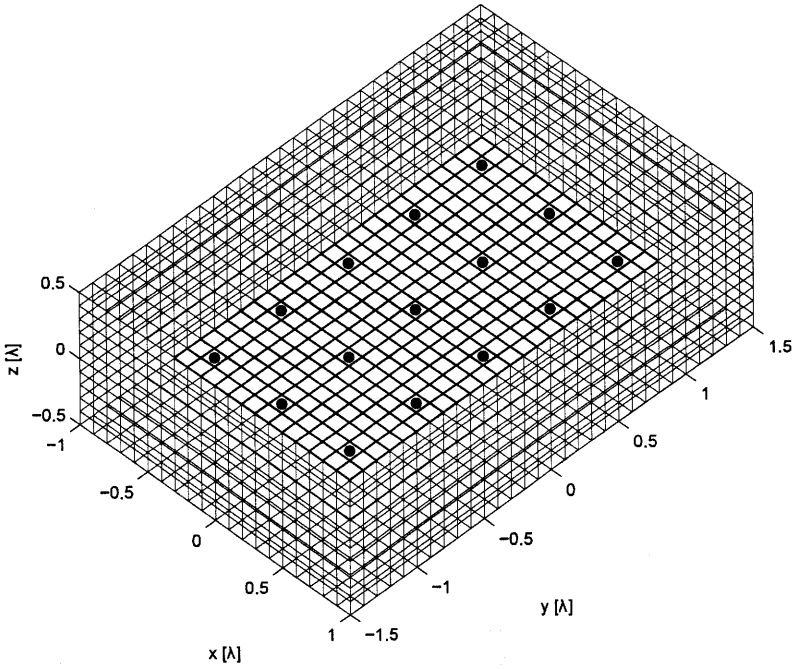

Figure 1.14: N2F bounding parallelepiped and 3 by 5 point sources, with $\lambda/10$ sampling resolution.

Resolution	Sphere samples	Sphere error	Box samples	Box error
$\lambda/2$	180	$2.11\ 10^{-1}$	88	$1.61\ 10^{-1}$
$\lambda/4$	760	$1.4\ 10^{-2}$	352	$1.68\ 10^{-2}$
$\lambda/8$	3 159	$3.09\ 10^{-3}$	1 408	$3.71\ 10^{-3}$
$\lambda/16$	12 960	$7.24\ 10^{-4}$	5 632	$9.01\ 10^{-4}$
$\lambda/32$	52 325	$1.78\ 10^{-4}$	22 528	$2.24\ 10^{-4}$
$\lambda/64$	210 600	$4.39\ 10^{-5}$	90 112	$5.58\ 10^{-5}$
$\lambda/128$	844 349	$1.09\ 10^{-5}$	360 448	$1.39\ 10^{-5}$

Table 1.1: Plotted values of figure 1.15.

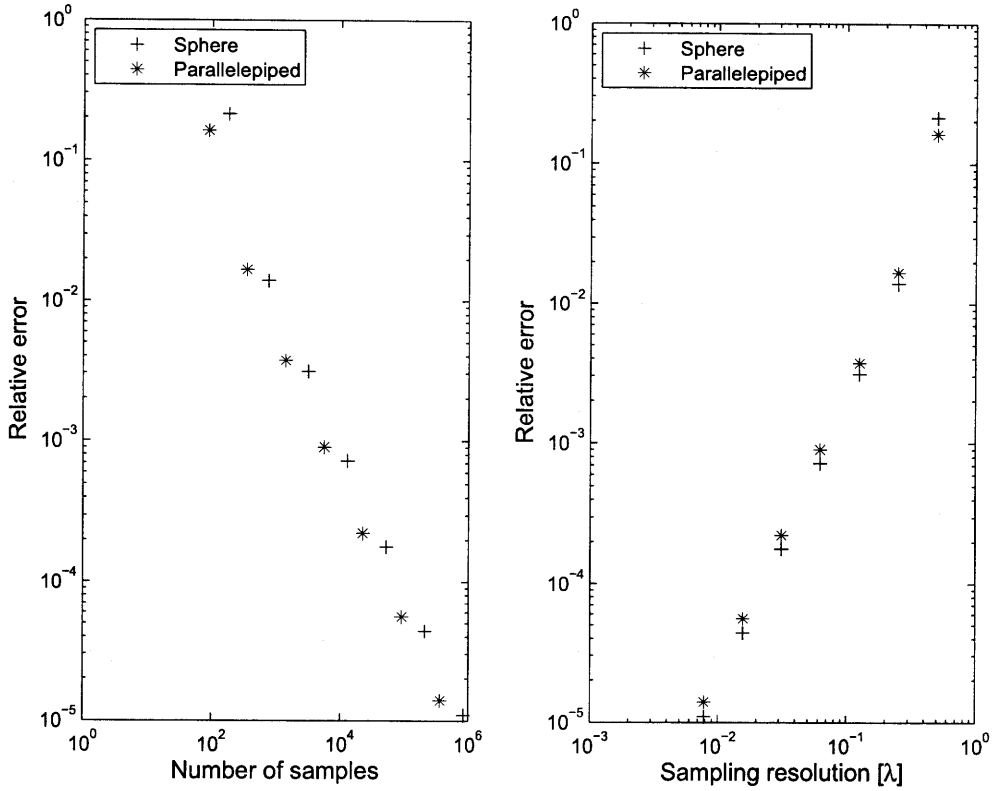

Figure 1.15: Near fields sampling points comparisons between the one required by the sphere and those for the parallelepiped for the 3 by 5 point sources array.

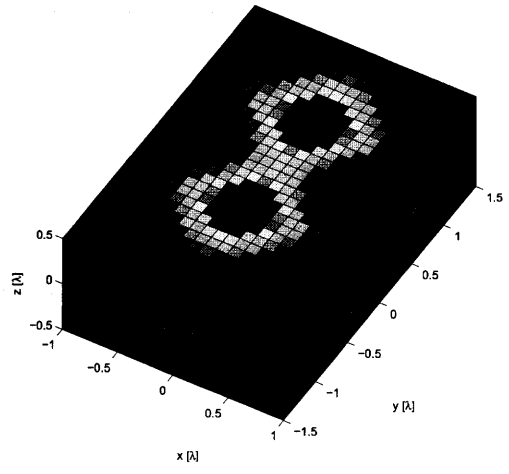

Figure 1.16: Near fields intensity $|\tilde{\psi}_m(\boldsymbol{r}'_m;\omega)|$ on the box with faces $\lambda/2$ away from the point sources.

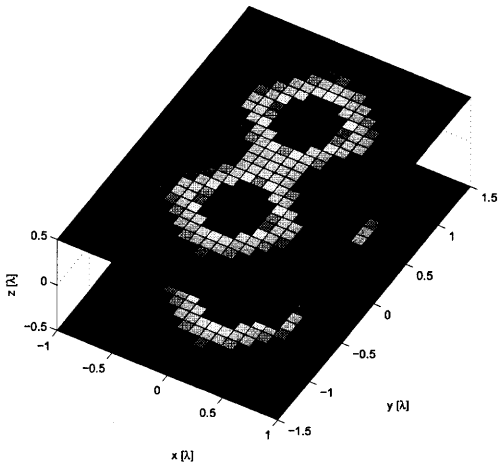

Figure 1.17: Near fields intensity on the top and bottom faces.

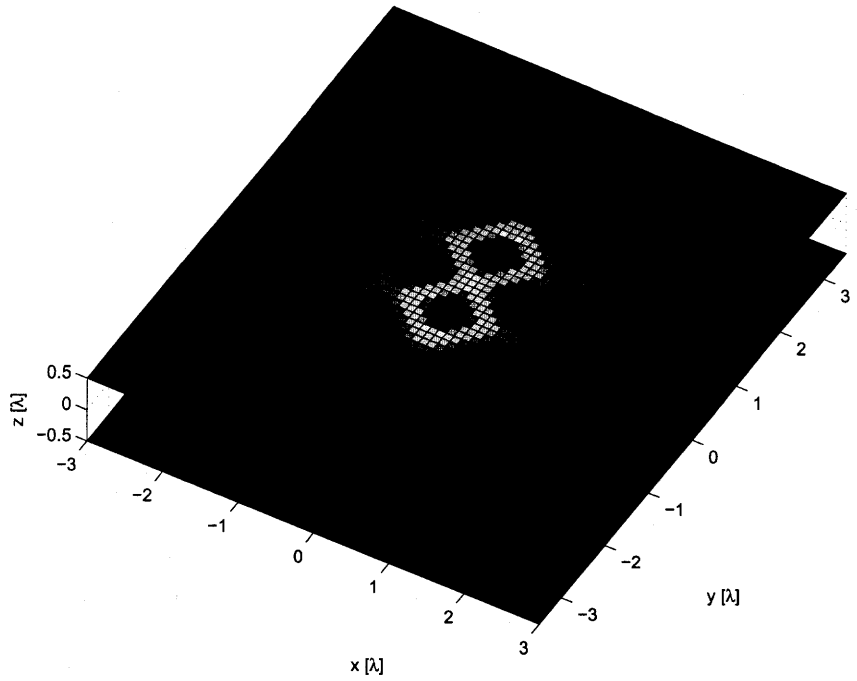

Figure 1.18: Top and bottom planes for truncated surface computation. Lateral extension from the edge point sources is set to 2.5λ.

reduce the fields intensities on those faces increasing the top and bottom planes dimensions as shown in figure 1.18. The omitted edge faces of the box have been set to lie 2.5λ away from the point sources located at the corners of the array. The patterns computed from the two planes are depicted in figures 1.19 and 1.20. The main lobe results to be accurately matched, and the error grows as we move to *end fire* ($\pm$ 90°) look angles : the total pattern error is of $\varepsilon_{[\lambda/10]} = 0.214$. It is clear that with this configuration, the scan angles will be restricted to a lower range around the broadside direction in order to preserve the main lobe accuracy, and an increase in the planes dimensions results into a wider range. However this increases the memory requirements, leading into a less numerically efficient configuration, especially for very large arrays (50 by 50 radiating elements for example).

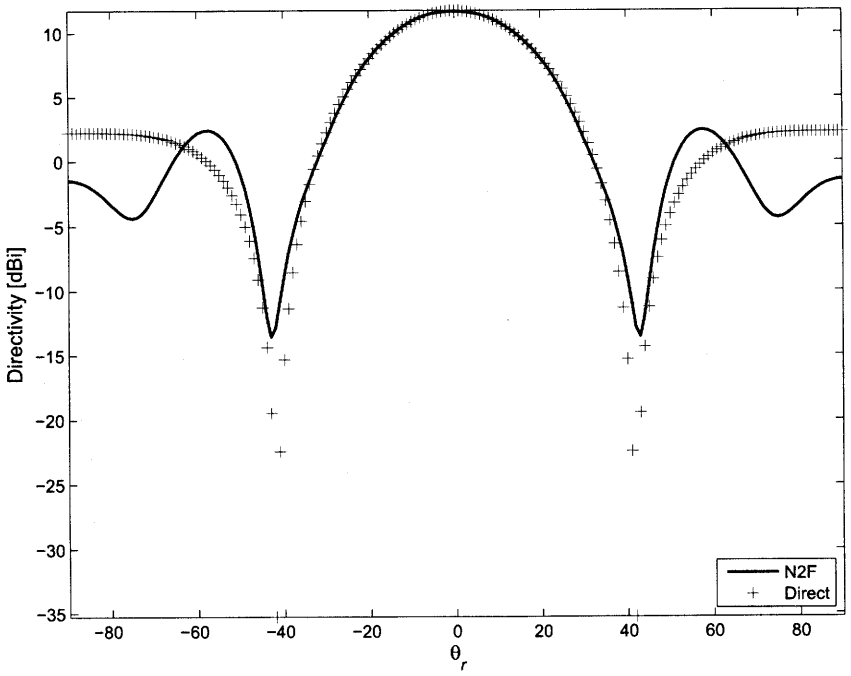

Figure 1.19: Pattern computed from the top and bottom faces of the box on the $\phi = 0°$ cut plane ($\lambda/10$ sampling resolution).

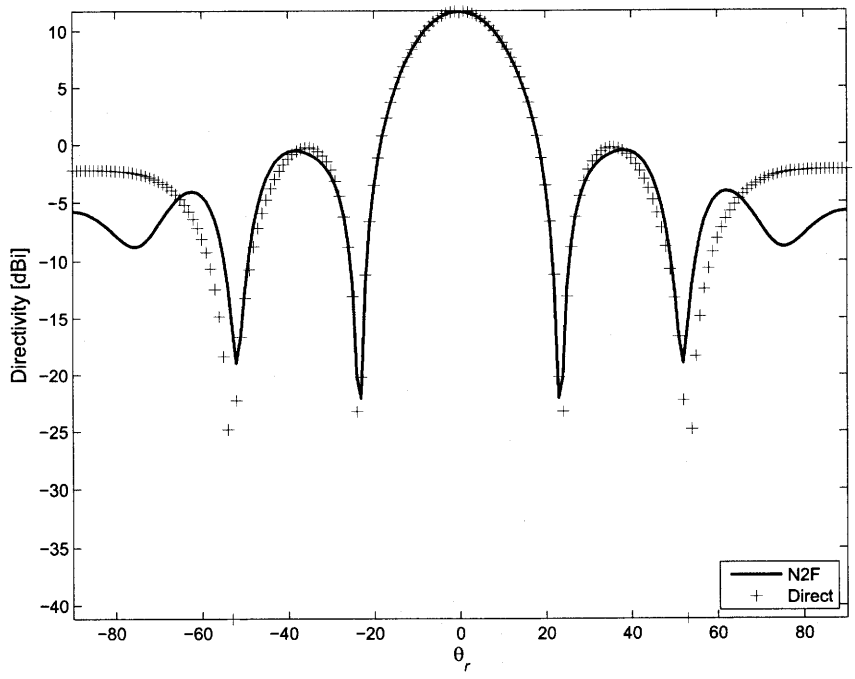

Figure 1.20: Pattern computed from the top and bottom faces of the box on the $\phi = 90°$ cut plane ($\lambda/10$ sampling resolution).

1.3 Vector fields near-to-far transformations

In this section, we present a numerical implementation of the near-to-far vector fields transformations (vector N2F), relying on the mathematical formulation discussed in section 1.1.4. The computation steps are the same as discussed in section 1.2.1. The results of an implementation in Matlab environment will be shown, considering as enclosing surface a parallelepiped. These results will be compared to ones obtained by means of the commercial CAD FEKO[14].

1.3.1 Direct computation of fields from current sources

The Kottler's formulas (1.1.73-1.1.74) contains informations on both direct fields computations (first integral) and on N2F fields computations (second integral). To numerically evaluate the vector N2F, we have chosen to enclose an array of 3 by 5 *Huygens' sources* [3] with a box, in a similar manner as it has been done in section 1.2.3. Huygens' sources are made of an infinitesimal electric current $\tilde{\boldsymbol{J}}(\boldsymbol{r}';\omega)$ crossing perpendicularly an infinitesimal magnetic current $\tilde{\boldsymbol{J}}_m(\boldsymbol{r}';\omega)$. The amplitude of the magnetic current has to be ζ times bigger to achieve the same radiated power than the electric one. Hugens' sources are constructed as if they where derived from far fields (plane wave behavior) and applying the equivalence principle (analog to Huygens' principle with equivalent currents, from which the name given to the sources). Now, to build the array, we have chosen the electric currents to be directed in $-\hat{\boldsymbol{y}}$ and the magnetic ones in $\hat{\boldsymbol{x}}$, such that the main radiation lobe is to be $\hat{\boldsymbol{z}}$-directed. Thus, we can express the currents of the array as

$$\tilde{\boldsymbol{J}}(\boldsymbol{r}';\omega) = -\tilde{J}\delta(\boldsymbol{r}-\boldsymbol{r}')\hat{\boldsymbol{y}} \tag{1.3.98}$$

$$\tilde{\boldsymbol{J}}_m(\boldsymbol{r}';\omega) = \zeta\tilde{J}_m\delta(\boldsymbol{r}-\boldsymbol{r}')\hat{\boldsymbol{x}} \tag{1.3.99}$$

where $\delta(\boldsymbol{r}-\boldsymbol{r}')$ is the Dirac delta, with its well known sifting property of integrals.

[14] FEKO© EM Software & Systems. Further informations available on `www.feko.info`.

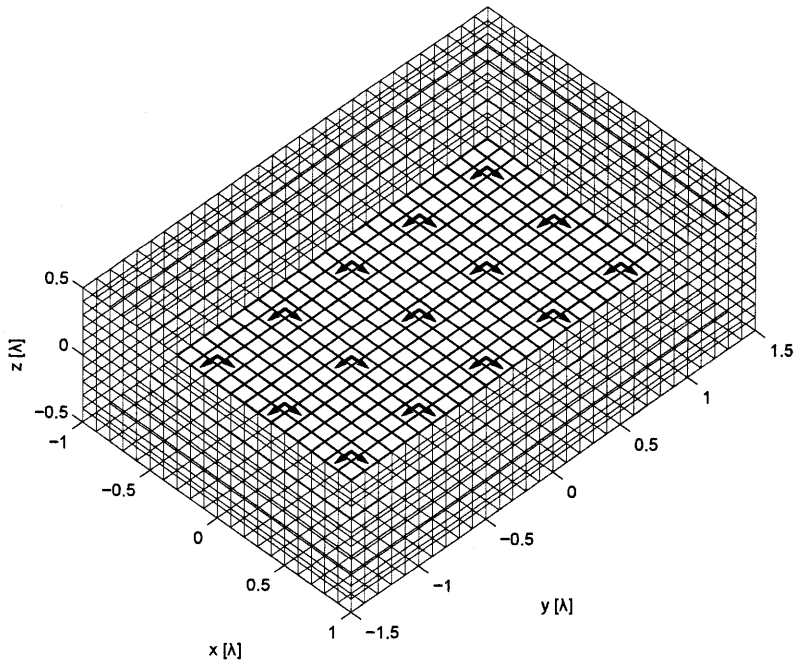

Figure 1.21: N2F bounding parallelepiped and 3 by 5 Huygens' sources, with $\lambda/10$ sampling resolution.

Let us now express analytically the terms involved with the Green's function (1.2.76) in the first integrals of Kottler's equations. Using the relation

$$\nabla G(\boldsymbol{r}|\boldsymbol{r}';\omega) = -\nabla' G(\boldsymbol{r}|\boldsymbol{r}';\omega) = \hat{\boldsymbol{R}}\frac{\partial}{\partial R}G(R;\omega), \tag{1.3.100}$$

with

$$G(\boldsymbol{r}|\boldsymbol{r}';\omega) = \frac{\mathrm{e}^{-jk|\boldsymbol{r}-\boldsymbol{r}'|}}{4\pi|\boldsymbol{r}-\boldsymbol{r}'|} = \frac{\mathrm{e}^{-jkR}}{4\pi R} = G(R;\omega),$$

we have

$$\nabla' G(\boldsymbol{r}|\boldsymbol{r}';\omega) = \left(jk + \frac{1}{R}\right)\frac{\mathrm{e}^{-jkR}}{4\pi R}\hat{\boldsymbol{R}}. \tag{1.3.101}$$

We need now to express explicitly the local gradient of (1.3.101) [11], which is a vector-valued function of R. To do this, we express in spherical components the gradient operator to evaluate $\nabla A_R(R)\hat{\boldsymbol{R}}$, A_R being the radial component of a vector-valued function $\boldsymbol{A}$ of R, where the transverse components A_θ and A_ϕ are null. We obtain

$$\nabla \boldsymbol{A}(R) = \left(\hat{\boldsymbol{R}}\frac{\partial}{\partial R} + \hat{\boldsymbol{\theta}}\frac{1}{R}\frac{\partial}{\partial \theta} + \hat{\boldsymbol{\phi}}\frac{1}{R\sin(\theta)}\frac{\partial}{\partial \phi}\right)A_R\hat{\boldsymbol{R}}$$

$$
\begin{aligned}
&= \hat{\boldsymbol{R}}\frac{\partial}{\partial R}A_R\hat{\boldsymbol{R}} + \hat{\boldsymbol{\theta}}\frac{1}{R}\frac{\partial}{\partial\theta}A_R\hat{\boldsymbol{R}} + \hat{\boldsymbol{\phi}}\frac{1}{R\sin(\theta)}\frac{\partial}{\partial\phi}A_R\hat{\boldsymbol{R}} \\
&= \hat{\boldsymbol{R}}\hat{\boldsymbol{R}}\frac{\partial}{\partial R}A_R + \hat{\boldsymbol{\theta}}\hat{\boldsymbol{\theta}}\frac{1}{R}A_R + \hat{\boldsymbol{\phi}}\hat{\boldsymbol{\phi}}\frac{1}{R}A_R, \qquad (1.3.102)
\end{aligned}
$$

where we have made the substitutions $\dfrac{\partial\hat{\boldsymbol{R}}}{\partial\theta} = \hat{\boldsymbol{\theta}}$ and $\dfrac{1}{\sin(\theta)}\dfrac{\partial\hat{\boldsymbol{R}}}{\partial\phi} = \hat{\boldsymbol{\phi}}$. With the use of the *identity dyadic* $\overline{\overline{I}} = \hat{\boldsymbol{R}}\hat{\boldsymbol{R}} + \hat{\boldsymbol{\theta}}\hat{\boldsymbol{\theta}} + \hat{\boldsymbol{\phi}}\hat{\boldsymbol{\phi}} = \hat{\boldsymbol{x}}\hat{\boldsymbol{x}} + \hat{\boldsymbol{y}}\hat{\boldsymbol{y}} + \hat{\boldsymbol{z}}\hat{\boldsymbol{z}}$ in both spherical and Cartesian components, equation (1.3.102) can be rewritten as

$$
\nabla\boldsymbol{A}(R) = \hat{\boldsymbol{R}}\hat{\boldsymbol{R}}\frac{\partial}{\partial R}A_R + \left(\overline{\overline{I}} - \hat{\boldsymbol{R}}\hat{\boldsymbol{R}}\right)\frac{1}{R}A_R. \qquad (1.3.103)
$$

Now, $\boldsymbol{A}(R)$ is substituted by $\nabla' G(\boldsymbol{r}|\boldsymbol{r}';\omega)$ and using (1.3.100) we can write

$$
\nabla'\nabla' G(\boldsymbol{r}|\boldsymbol{r}';\omega) = -\left(\hat{\boldsymbol{R}}\hat{\boldsymbol{R}}\frac{\partial}{\partial R} + \left(\overline{\overline{I}} - \hat{\boldsymbol{R}}\hat{\boldsymbol{R}}\right)\frac{1}{R}\right)\left(jk + \frac{1}{R}\right)\frac{\mathrm{e}^{-jkR}}{4\pi R}. \qquad (1.3.104)
$$

Noting that $\tilde{\boldsymbol{J}}\cdot\overline{\overline{I}} = \tilde{\boldsymbol{J}}$, Kottler's equations for an unbounded medium can be rewritten as, with $G = G(R;\omega)$,

$$
\begin{aligned}
\tilde{\boldsymbol{E}}(\boldsymbol{r};\omega) &= \frac{1}{j\omega\epsilon}\int_V \left[\tilde{\boldsymbol{J}}\left(k^2 - \frac{jk}{R} - \frac{1}{R^2}\right)G + \left(\tilde{\boldsymbol{J}}\cdot\hat{\boldsymbol{R}}\right)\hat{\boldsymbol{R}}\left(-k^2 + \frac{3jk}{R} + \frac{3}{R^2}\right)G - \right. \\
&\qquad \left. j\omega\epsilon\tilde{\boldsymbol{J}}_m\times\hat{\boldsymbol{R}}\left(jk + \frac{1}{R}\right)G\right]dV' \\
&= \frac{\zeta k^2}{4\pi}\int_V \left[\tilde{\boldsymbol{J}}\left(-\frac{j}{kR} - \frac{1}{k^2R^2} + \frac{j}{k^3R^3}\right) + \left(\tilde{\boldsymbol{J}}\cdot\hat{\boldsymbol{R}}\right)\hat{\boldsymbol{R}}\left(\frac{j}{kR} + \frac{3}{k^2R^2} - \frac{3j}{k^3R^3}\right) - \right. \\
&\qquad \left. \frac{1}{\zeta}\tilde{\boldsymbol{J}}_m\times\hat{\boldsymbol{R}}\left(\frac{j}{kR} + \frac{1}{k^2R^2}\right)\right]\mathrm{e}^{-jkR}dV', \qquad (1.3.105)
\end{aligned}
$$

$$
\begin{aligned}
\tilde{\boldsymbol{H}}(\boldsymbol{r};\omega) &= \frac{1}{j\omega\mu}\int_V \left[\tilde{\boldsymbol{J}}_m\left(k^2 - \frac{jk}{R} - \frac{1}{R^2}\right)G + \left(\tilde{\boldsymbol{J}}_m\cdot\hat{\boldsymbol{R}}\right)\hat{\boldsymbol{R}}\left(-k^2 + \frac{3jk}{R} + \frac{3}{R^2}\right)G + \right. \\
&\qquad \left. j\omega\mu\tilde{\boldsymbol{J}}\times\hat{\boldsymbol{R}}\left(jk + \frac{1}{R}\right)G\right]dV' \\
&= \frac{k^2}{4\pi\zeta}\int_V \left[\tilde{\boldsymbol{J}}_m\left(-\frac{j}{kR} - \frac{1}{k^2R^2} + \frac{j}{k^3R^3}\right) + \right. \\
&\qquad \left(\tilde{\boldsymbol{J}}_m\cdot\hat{\boldsymbol{R}}\right)\hat{\boldsymbol{R}}\left(\frac{j}{kR} + \frac{3}{k^2R^2} - \frac{3j}{k^3R^3}\right) + \\
&\qquad \left. \zeta\,\tilde{\boldsymbol{J}}\times\hat{\boldsymbol{R}}\left(\frac{j}{kR} + \frac{1}{k^2R^2}\right)\right]\mathrm{e}^{-jkR}dV'. \qquad (1.3.106)
\end{aligned}
$$

We can now compute the fields on the bounding surface, integrating over the volume enclosed and using the sifting property of the Dirac delta. The integration is

done considering each vector component separately in a Cartesian coordinates system. Also, using the far fields approximation of the Green's function by (1.2.85), one can compute the pattern directly from the sources distribution.

1.3.2 Near to far fields computations

The second integral term of Kottler's equations (1.1.73-1.1.74) can be straightforwardly obtained from (1.3.105-1.3.106), assuming the current terms to be equivalent currents on the bounding surface, such that the volume integrals reduce into surface integrals. Thus, we have

$$\begin{aligned}\tilde{\boldsymbol{E}}(\boldsymbol{r};\omega) &= \frac{\zeta k^2}{4\pi}\oint_{S_0}\left[\tilde{\boldsymbol{J}}_s^{eq}\left(-\frac{j}{kR}-\frac{1}{k^2R^2}+\frac{j}{k^3R^3}\right)+\right.\\ &\quad\left(\tilde{\boldsymbol{J}}_s^{eq}\cdot\hat{\boldsymbol{R}}\right)\hat{\boldsymbol{R}}\left(\frac{j}{kR}+\frac{3}{k^2R^2}-\frac{3j}{k^3R^3}\right)-\\ &\quad\left.\frac{1}{\zeta}\,\tilde{\boldsymbol{J}}_{ms}^{eq}\times\hat{\boldsymbol{R}}\left(\frac{j}{kR}+\frac{1}{k^2R^2}\right)\right]\mathrm{e}^{-jkR}\,dS', \qquad (1.3.107)\end{aligned}$$

$$\begin{aligned}\tilde{\boldsymbol{H}}(\boldsymbol{r};\omega) &= \frac{k^2}{4\pi\zeta}\oint_{S_0}\left[\tilde{\boldsymbol{J}}_{ms}^{eq}\left(-\frac{j}{kR}-\frac{1}{k^2R^2}+\frac{j}{k^3R^3}\right)+\right.\\ &\quad\left(\tilde{\boldsymbol{J}}_{ms}^{eq}\cdot\hat{\boldsymbol{R}}\right)\hat{\boldsymbol{R}}\left(\frac{j}{kR}+\frac{3}{k^2R^2}-\frac{3j}{k^3R^3}\right)+\\ &\quad\left.\zeta\,\tilde{\boldsymbol{J}}_s^{eq}\times\hat{\boldsymbol{R}}\left(\frac{j}{kR}+\frac{1}{k^2R^2}\right)\right]\mathrm{e}^{-jkR}\,dS', \qquad (1.3.108)\end{aligned}$$

where $\tilde{\boldsymbol{J}}_s^{eq}=\tilde{\boldsymbol{J}}_s^{eq}(\boldsymbol{r}';\omega)=\hat{\boldsymbol{n}}\times\tilde{\boldsymbol{H}}(\boldsymbol{r}';\omega)$ and $\tilde{\boldsymbol{J}}_{ms}^{eq}=\tilde{\boldsymbol{J}}_{ms}^{eq}(\boldsymbol{r}';\omega)=-\hat{\boldsymbol{n}}\times\tilde{\boldsymbol{E}}(\boldsymbol{r}';\omega)$. With the far fields approximation of the Green's function (1.2.85), the second integral term of Kottler's equations (1.3.107-1.3.108) become

$$\tilde{\boldsymbol{E}}(\boldsymbol{r};\omega)\Big|_{r\gg r'} \approx j\zeta k\frac{\mathrm{e}^{-jkr}}{4\pi r}\oint_{S_0}\mathrm{e}^{jk\hat{\boldsymbol{r}}\cdot\boldsymbol{r}'}\left[-\tilde{\boldsymbol{J}}_s^{eq}+\left(\tilde{\boldsymbol{J}}_s^{eq}\cdot\hat{\boldsymbol{r}}\right)\hat{\boldsymbol{r}}-\frac{1}{\zeta}\,\tilde{\boldsymbol{J}}_{ms}^{eq}\times\hat{\boldsymbol{r}}\right]dS' \qquad (1.3.109)$$

$$\tilde{\boldsymbol{H}}(\boldsymbol{r};\omega)\Big|_{r\gg r'} \approx j\frac{k}{\zeta}\frac{\mathrm{e}^{-jkr}}{4\pi r}\oint_{S_0}\mathrm{e}^{jk\hat{\boldsymbol{r}}\cdot\boldsymbol{r}'}\left[-\tilde{\boldsymbol{J}}_{ms}^{eq}+\left(\tilde{\boldsymbol{J}}_{ms}^{eq}\cdot\hat{\boldsymbol{r}}\right)\hat{\boldsymbol{r}}+\zeta\,\tilde{\boldsymbol{J}}_s^{eq}\times\hat{\boldsymbol{r}}\right]dS' \qquad (1.3.110)$$

1.3.3 Radiation pattern

With (1.3.109-1.3.110), we can now derive the far fields pattern. As the computations are done considering the Cartesian components of the currents $\tilde{\boldsymbol{J}}$ and $\tilde{\boldsymbol{J}}_m$, or

$\tilde{\boldsymbol{J}}_s^{eq}$ and $\tilde{\boldsymbol{J}}_{ms}^{eq}$ in the vector N2F, the Cartesian components of the unit vector $\hat{\boldsymbol{R}} \underset{r\gg r'}{\approx} \hat{\boldsymbol{r}}$, the resulting far fields detectors $\tilde{\boldsymbol{E}}^*$ and $\tilde{\boldsymbol{H}}^*$ are in Cartesian components : $\tilde{\boldsymbol{E}}_x^*$, $\tilde{\boldsymbol{E}}_y^*$, $\tilde{\boldsymbol{E}}_z^*$ and $\tilde{\boldsymbol{H}}_x^*$, $\tilde{\boldsymbol{H}}_y^*$, $\tilde{\boldsymbol{H}}_z^*$. To simplify the pattern computations, these can be converted into spherical components[15] and discard the radial components $\tilde{\boldsymbol{E}}_r^*$ and $\tilde{\boldsymbol{H}}_r^*$ which must be null in the far zones. Furthermore, the plane wave behavior of the electromagnetic fields in the far zones, that is

$$\tilde{\boldsymbol{H}}^* = \frac{1}{\zeta}\hat{\boldsymbol{r}} \times \tilde{\boldsymbol{E}}^*, \tag{1.3.111}$$

allows us to keep either the electric field or the magnetic field to derive the pattern of the radiating structure. We have chosen to keep the electric field detectors $\tilde{\boldsymbol{E}}_\theta^*$ and $\tilde{\boldsymbol{E}}_\phi^*$ from which the gain can be obtained in term of θ and ϕ polarizations by the following expressions [3] [7]

$$\mathscr{P}_\theta(\hat{\boldsymbol{r}};\omega) = \lim_{r\to\infty} 4\pi r^2 \frac{S_{r[\theta]}}{\mathrm{P}_r} = 4\pi \frac{\left|\tilde{\boldsymbol{E}}_\theta^*\right|^2}{2\zeta \mathrm{P}_r} = 2\pi \frac{\left|\tilde{\boldsymbol{E}}_\theta^*\right|^2}{\zeta \mathrm{P}_r}, \tag{1.3.112}$$

$$\mathscr{P}_\phi(\hat{\boldsymbol{r}};\omega) = \lim_{r\to\infty} 4\pi r^2 \frac{S_{r[\phi]}}{\mathrm{P}_r} = 4\pi \frac{\left|\tilde{\boldsymbol{E}}_\phi^*\right|^2}{2\zeta \mathrm{P}_r} = 2\pi \frac{\left|\tilde{\boldsymbol{E}}_\phi^*\right|^2}{\zeta \mathrm{P}_r}, \tag{1.3.113}$$

where $S_{r[\theta]}$ and $S_{r[\phi]}$ are the active power densities related to each of the polarizations[16]. The term P_r is the radiated power that, for practical reasons, has to be computed from the fields on the bounding surface. In effect, we could compute the total power using the far fields detectors, selecting the appropriate number of look angles to cover a sphere, but this is excessively time consuming. The computation of the power radiated from the near fields is achieved by an integration of the flux of the Poynting vector and keeping half of the real part. In other terms

$$\begin{aligned} \mathrm{P}_r &= \frac{1}{2}\Re\left\{\oint_{S_0} \boldsymbol{S}_r(\boldsymbol{r}';\omega)\cdot\hat{\boldsymbol{n}}\, dS'\right\} \\ &= \frac{1}{2}\Re\left\{\oint_{S_0} \left[\tilde{\boldsymbol{E}}(\boldsymbol{r}';\omega)\times\tilde{\boldsymbol{H}}^\dagger(\boldsymbol{r}';\omega)\right]\cdot\hat{\boldsymbol{n}}\, dS'\right\} \end{aligned} \tag{1.3.114}$$

[15] $\boldsymbol{A}_r = \boldsymbol{A}_x\sin(\theta)\cos(\phi) + \boldsymbol{A}_y\sin(\theta)\sin(\phi) + \boldsymbol{A}_z\cos(\theta)$, $\boldsymbol{A}_\theta = \boldsymbol{A}_x\cos(\theta)\cos(\phi) + \boldsymbol{A}_y\cos(\theta)\sin(\phi) - \boldsymbol{A}_z\sin(\theta)$ and $\boldsymbol{A}_\phi = -\boldsymbol{A}_x\sin(\phi) + \boldsymbol{A}_y\cos(\phi)$. [1]

[16] Real part of the radial component of the *Poynting vector*, the first due to θ-polarized electric field and the second due to ϕ-polarized electric field.

where the symbol † indicates the complex conjugate. The total pattern, polarization independent, is given by

$$\mathscr{P}(\hat{\boldsymbol{r}};\omega) = \mathscr{P}_\theta(\hat{\boldsymbol{r}};\omega) + \mathscr{P}_\phi(\hat{\boldsymbol{r}};\omega). \tag{1.3.115}$$

1.3.4 Numerical results

We proceed with the numerical implementation that solves the vector N2F on the array depicted in figure 1.21, comparing it to results obtained with FEKO. All the surface integrals have been computed by means of numerical midpoint integrations for each vector component separately, in a similar manner as it was done for scalar fields in section 1.2 (see note 11). Figure 1.22 shows the power density on the box surface, computed by our implementation. Notice that, as the sources are not radiating isotropically but mainly along the $\hat{\boldsymbol{z}}$ direction, the level of the fields on the lateral faces of the box is low when compared to those generated by point sources (figure 1.16). In order to compare our implementation results to FEKO's ones, the frequency of the sources has been set to 1 GHz in both simulation environments. Also. the electric currents are set to be of 1 [A] and the magnetic currents are of $\zeta \approx 376.73$ [V]. The FEKO model of the array analyzed is depicted in figure 1.23.

The patterns on the XZ and YZ cut planes computed with FEKO are shown in figures 1.24 and 1.25. Both of them are the total fields directivity patterns (no polarization splitting) and they have a maximum value of 16.474 [dBi] on the broadside direction. The total power radiated by the array, for FEKO, is of $1.3346\ 10^5$ [W], while our implementation gives $1.33528\ 10^5$ [W] with $\lambda/10$ of sampling resolution on the box, that is -0.051 % of relative error. Notice that errors in the power radiated computation can vary sensibly the maximum gain, but not the pattern shape. The total pattern achieved with our implementation is depicted in figure 1.26. The maximum gain achieved is of 16.481 [dBi], slightly higher than the one computed by FEKO, and this is mainly due to the misfit in the power radiated (coarse integration of the power density on the box). In effect, as we will see below, the error on the fields detectors resulted to be very low. However, for practical applications, that error can be consid-

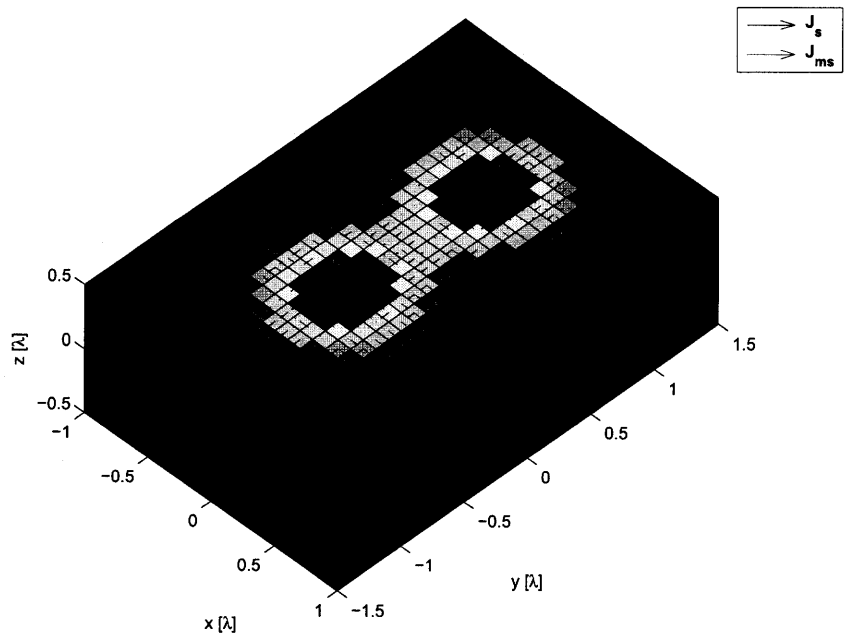

Figure 1.22: Surface power density and real part of the equivalent currents computed on the box of figure 1.21.

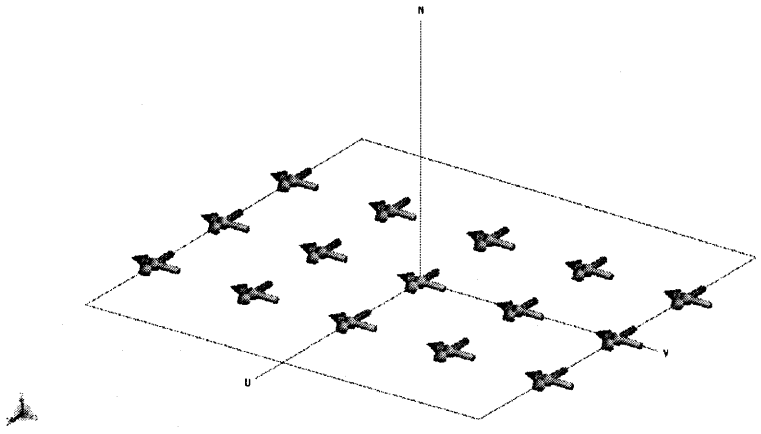

Figure 1.23: FEKO model of the 3 by 5 Huygens' sources array of figure 1.21.

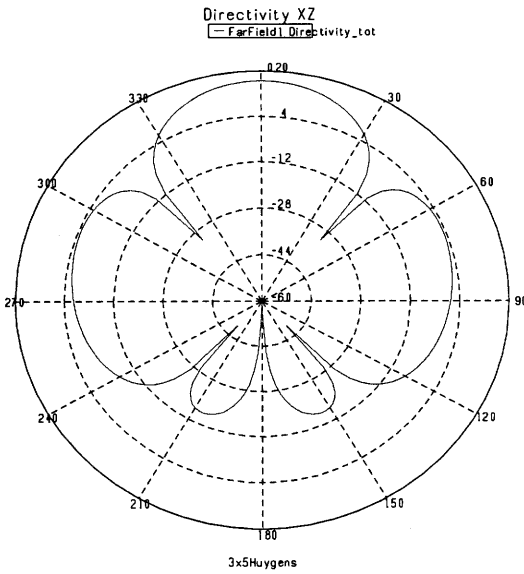

Figure 1.24: Pattern computed with FEKO on the $\phi = 0°$ cut plane.

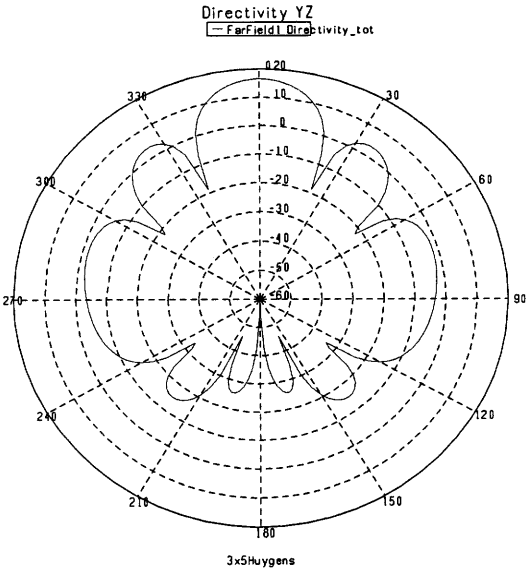

Figure 1.25: Pattern computed with FEKO on the $\phi = 90°$ cut plane.

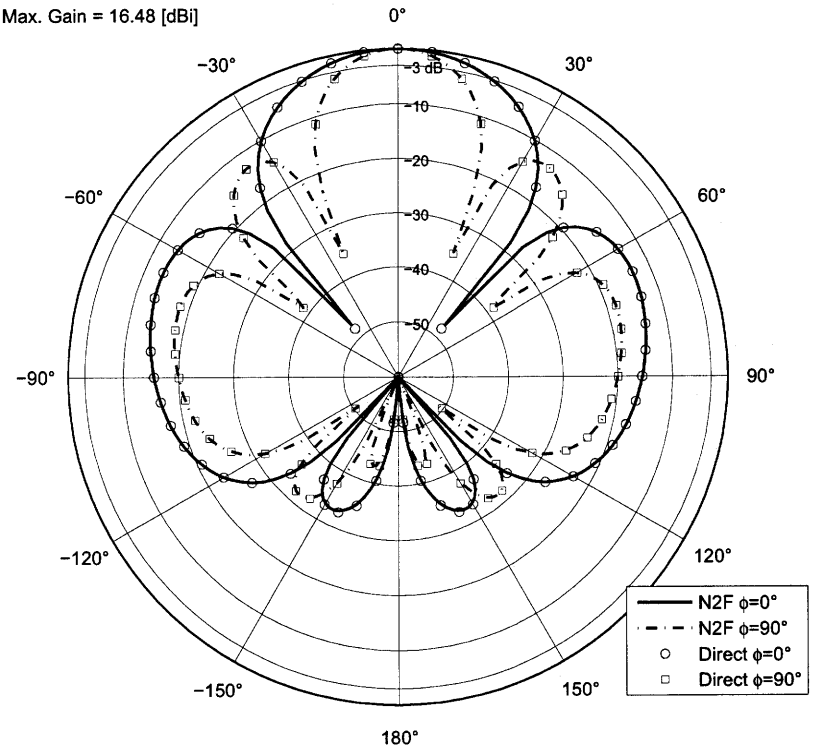

Figure 1.26: N2F and direct total fields patterns computed for the array of figure 1.22.

ered to be low enough and the pattern sufficiently accurate.

The pattern formulation has been split into θ and ϕ polarizations, and this allows us to evaluate the cross-polarizations behavior of real antenna. Plots of $\mathscr{P}_\theta\left(\hat{\boldsymbol{r}};\omega\right)$ and $\mathscr{P}_\phi\left(\hat{\boldsymbol{r}};\omega\right)$ are given in figures 1.27 and 1.28.

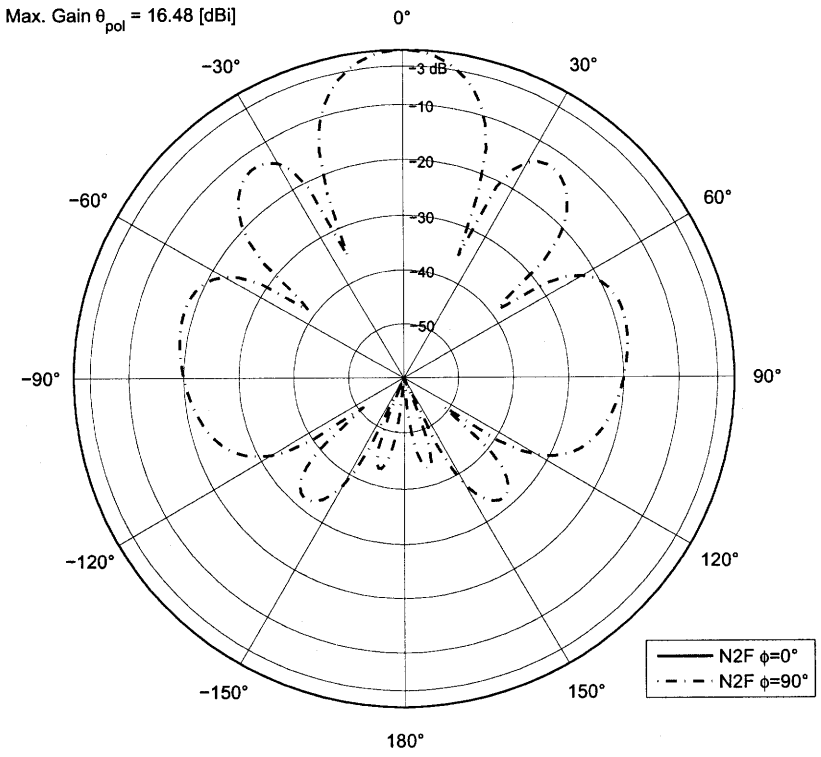

Figure 1.27: θ polarization pattern $\mathscr{P}_\theta\left(\hat{\boldsymbol{r}};\omega\right)$ of the 3 by 5 Huygens sources array.

Let us now quantify the error between the patterns computed by N2F and direct processes, using the following relation, similarly to 1.2.96,

$$\varepsilon_{[\text{Direct}-\text{N2F}]} = \frac{\left\| \left(\tilde{\boldsymbol{E}}^*_{\text{Direct}\theta} + \tilde{\boldsymbol{E}}^*_{\text{Direct}\phi}\right) - \left(\tilde{\boldsymbol{E}}^*_{\text{N2F}\theta} + \tilde{\boldsymbol{E}}^*_{\text{N2F}\phi}\right) \right\|_2}{\left\| \tilde{\boldsymbol{E}}^*_{\text{Direct}\theta} + \tilde{\boldsymbol{E}}^*_{\text{Direct}\phi} \right\|_2}. \quad (1.3.116)$$

The FEKO results have been compared first to those of the direct computation using (1.3.116). The error in this case is of $\varepsilon_{[\text{Direct}-\text{FEKO}]} = 1.487\ 10^{-4}$, which significantly validates our implementation. Then, comparing them to the N2F results, we have $\varepsilon_{[\text{N2F}\ [\lambda/10]-\text{FEKO}]} = 1.821\ 10^{-3}$. Finally, as we expected, the error committed in the N2F computation with $\lambda/10$ sampling resolution on the box, relatively to the direct

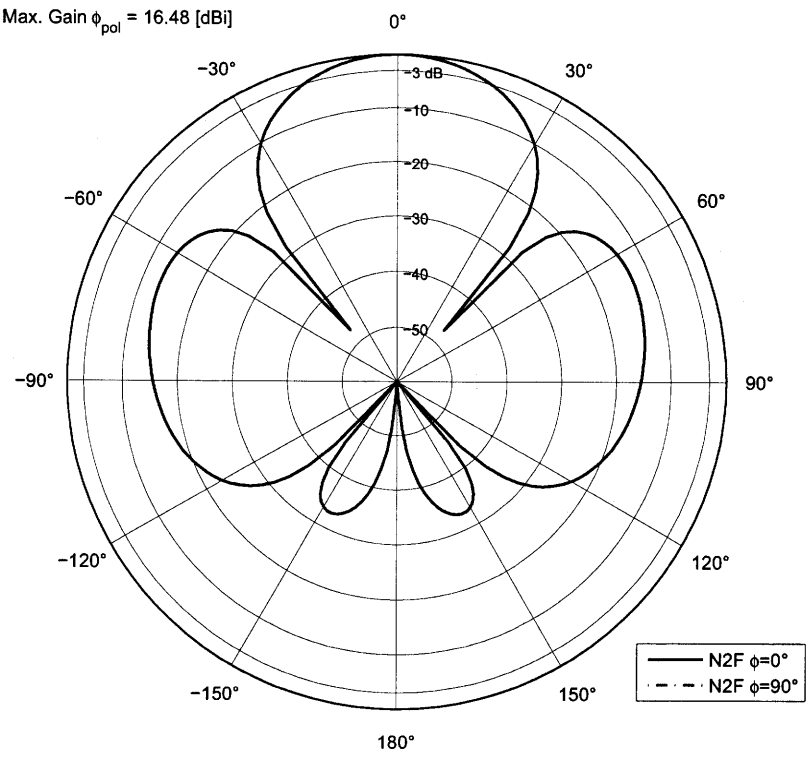

Figure 1.28: ϕ polarization pattern $\mathscr{P}_{\phi}\left(\hat{\boldsymbol{r}};\omega\right)$ of the 3 by 5 Huygens sources array.

computation, is of $\varepsilon_{[\text{Direct}-\text{N2F}\ [\lambda/10]]} = \varepsilon_{[\lambda/10]} = 1.842\ 10^{-3}$, similar to $\varepsilon_{[\text{N2F}\ [\lambda/10]-\text{FEKO}]}$ as $\varepsilon_{[\text{Direct}-\text{FEKO}]}$ is of an order below. Also, notice that the N2F error is of the same order that one computed for scalar fields in section 1.2.2.2 ($2.398\ 10^{-3}$). Figure 1.29 shows the same convergence behavior of the vector N2F, analogously to the scalar N2F (1.15), while increasing the sampling resolution.

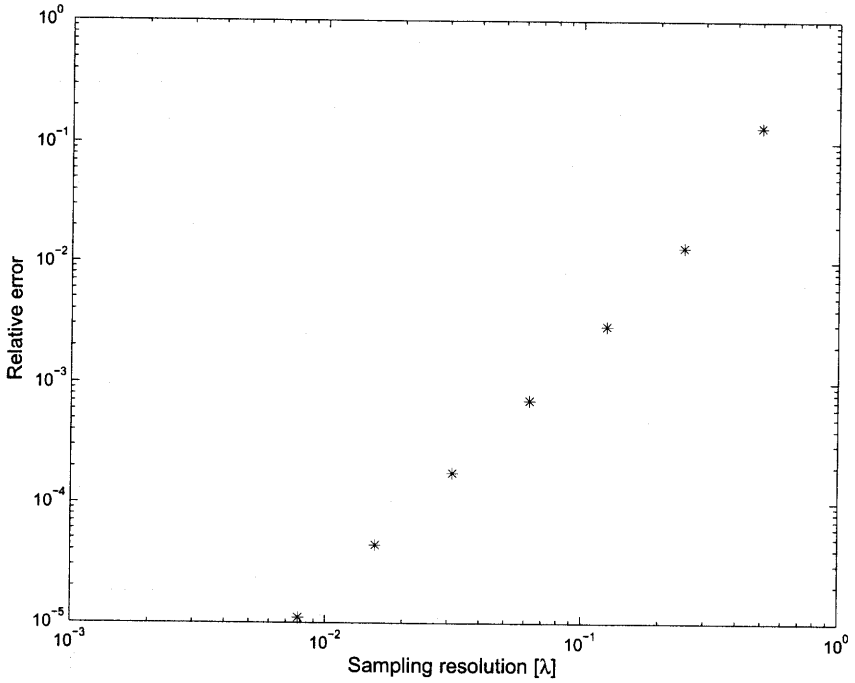

Figure 1.29: Relative error between N2F and direct far fields detectors for several sampling resolutions.